STRUCTURAL AND ELECTRICAL CHARACTERIZATION OF HIGHLY

ORIENTED (K_xNa_x)NbO_3 (KNN) THIN FILMS BY

CHEMICAL SOLUTION DEPOSITION

Except where reference is made to the work of others, the work described in this thesis is my own or was done in collaboration with my advisory committee. This thesis does not include proprietary or classified information.

_____
Chiwon Kang

Certificate of Approval:

_____
Minseo Park
Associate Professor
Physics

_____
Dong-Joo Kim, Chair
Associate Professor
Materials Engineering

_____
ZhongYang Cheng
Associate Professor
Materials Engineering

_____
George T. Flowers
Dean
Graduate School

STRUCTURAL AND ELECTRICAL CHARACTERIZATION OF HIGHLY

ORIENTED $(K_xNa_x)NbO_3$ (KNN) THIN FILMS BY

CHEMICAL SOLUTION DEPOSITION

Chiwon Kang

A Thesis

Submitted to

the Graduate Faculty of

Auburn University

in Partial Fulfillment of the

Requirement for the

Degree of

Master of Science

Auburn, Alabama
May 09, 2009

STRUCTURAL AND ELECTRICAL CHARACTERIZATION OF HIGHLY

ORIENTED $(K_xNa_x)NbO_3$ (KNN) THIN FILMS BY

CHEMICAL SOLUTION DEPOSITION

Chiwon Kang

_____
Signature of Author

_____
Date of Graduation

VITA

Chiwon Kang, son of Hoyeon Kang and Hyewon Kim, was born on March 26, 1976. He attended Yonsei University, Seoul, Korea and obtained a B.S. degree in Ceramic Engineering in 2001. After completion of master program of ceramic engineering at Yonsei University, he entered Auburn University and joined Dr. Kim's lab in spring 2007.

THESIS ABSTRACT

STRUCTURAL AND ELECTRICAL CHARACTERIZATION OF HIGHLY

ORIENTED $(K_xNa_x)NbO_3$ (KNN) THIN FILMS BY

CHEMICAL SOLUTION DEPOSITION

Chiwon Kang

Master of Science, May 09, 2009
(B.S. Ceramic Engineering, Yonsei University, South Korea, 2001)

98 Typed Pages

Directed by Dong-Joo Kim

$(K_{0.5}Na_{0.5})NbO_3$ (KNN) perovskite materials have been developed as promising lead-free piezoelectric materials for environmentally and biologically benign piezoelectric devices. To date, however, there are few reports on the growth of good KNN thin films by chemical solution deposition (CSD) and on their properties for device applications. Excellent crystallinity at low temperatures with a uniform and controllable microstructure is required for improvement of the electrical properties, including piezoelectric properties. KNN thin films were fabricated on $SiO_2/Si(100)$ and $Pt(111)/SiO_2/Si(100)$ substrates by chemical solution deposition. By applying different annealing conditions, highly oriented KNN was attained at 550 °C and above. The effects of the substrates on crystallographic orientation were not distinguishable in these films. However, the thickness of pyrolize

film strongly affects film orientation. For thinner pyrolized layers, KNN showed textured orientation due to the influence of interfaces between the Pt(111) layer and KNN, which served as heterogeneous nucleation sites. For thicker layers, homogeneous nucleation and growth were prevalent, thus resulting in random orientations. For $(K_{0.5}Na_{0.5})NbO_3$, typical P-E hysteresis loops could not be obtained due to the leakage current. Since the leakage current could stem from volatilization of Na and K ions at a higher temperature, the excessive Na and K were added in order to compensate for the volatile ones and sustain MPB composition of KNN. $K_{0.6}Na_{0.5}NbO_3$ could endure higher applied electric fields over 800 kV/cm showing reasonably typical P-E hysteresis curves. The maximum 2Pr and 2Ec values are approximately 17.5 $\mu C/cm^2$ and 150 kV/cm, respectively.

ACKNOWLEDGMENTS

I would like to express my respect and thanks to my advisor Dr. Dong-Joo Kim for his direction, patience, and encouragement which was invaluable during the entire time of this research. I am very grateful for the sincere support of Dr. Minseo Park and Dr. ZhongYang Cheng being on my thesis committee. I appreciate my research group members, Sang H. Yoon, Jung-Hyun Park, Dongna Shen, Dan Liu, Hosang Ahn, Jacob W. Craft, Ishita Banerjee, Seon-Bae Kim, Eun Soo Yang, Dr. Young Ho Kim, Dr. Joo Hyon Noh, and Dr. Howard C. Wikle III for their support and friendship. Finally, I give my sincere appreciation to my mother for providing help in numerous ways.

Style manual or journal used <u>Guide to Preparation and Submission of Theses and</u>

<u>Dissertations</u>

Computer software used <u>Microsoft Word 2003, Origin 7.5</u>

TABLE OF CONTENTS

LIST OF TABLES

LIST OF FIGURES

CHAPTER I

INTRODUCTION

1.1 Overview

Lead-free piezoelectric materials have been studied due to the environmental and biological advantages and comparable piezoelectric properties to PZT [1 - 4]. Despite its excellent piezoelectric properties, one of the major disadvantages of PZT is potential lead volatility at higher temperatures. It is known that lead poisoning can result in adverse effects on health such as reduced IQ, slowed body growth, and kidney damage [5].

$(K_{0.5}Na_{0.5})NbO_3$ (KNN) is currently considered as a promising candidate of lead-free piezoelectric materials. KNN is a solid solution of ferroelectric $KNbO_3$ (space group Amm2 (No. 38) with $a = 0.4027$ nm , $b = 0.4057$ nm and $c = 0.3914$ nm) and antiferroelectric $NaNbO_3$ (space group Pbcm (No. 57) with $a = 0.3950$ nm , $b = 0.3875$ nm and $c = 0.3914$ nm) [6]. KNN posseses an orthorhombic structure at room temperature. Recently, Saito et al. reported that most of the piezoelectric properties are comparable to those of PZT [1]. However, densification of KNN ceramics is reported to be difficult. Thin film fabrication of these materials is even more challenging due to added complexity in the process compared to bulk ceramic fabrication.

Growth of KNN-based thin films has been investigated by several methods such as pulsed laser deposition [7 - 8], aerosol deposited films [9], metal organic chemical vapor

deposition [10], radio frequency (rf) magnetron sputtering [11 - 16], and chemical solution deposition [17 - 21]. Among these methods, sol-gel processing (chemical solution deposition) is considered to be excellent due to the ability for mass production, composition control of complex oxides, and synthesis at lower temperatures. In particular, K. Tanaka *et al.* reported the fabrication of oriented KNN thin films on SiO_2/Si(100) substrates at temperatures ranging from 450°C to 700°C [18]. Y. Nakashima *et al.* reported the electrical properties of KNN thin films with excess K and Na deposited on a $Pt(111)/TiO_x/SiO_2/Si(100)$ substrate [19, 20]. However, to date, there are few reports on KNN thin film fabrication with obtaining controlled orientation on $Pt(111)/SiO_2/Si(100)$ and SiO_2/Si(100) substrates by chemical solution deposition. Excellent textured orientation at low temperature with a uniform and controllable microstructure can be an essential requirement for the improvement in electrical properties.

In the present study, several key processing parameters in the fabrication of KNN thin films on $Pt(111)/SiO_2/Si(100)$ and SiO_2/Si(100) substrates were investigated for their effects on the properties of KNN films. Thermal analysis of the KNN precursor gel was performed to observe the progressive stages of organic combustion and the subsequent crystallization of the KNN thin film, and the result was used to determine heat treatment conditions. The crystallization orientation and microstructure of the KNN thin film were strongly influenced by the thickness of the pyrolized layers and annealing temperatures. Furthermore, the electrical properties of the KNN thin films fabricated under the different annealing conditions were measured and compared. Finally, the excessive addition of K and Na ions in KNN films is systematically investigated.

1.2 Thesis Structure

Chapter 2 includes a literature survey from which this thesis work is based. The physical principles of piezoelectricity will be mainly dealt with. Also, the current applications of the piezoelectric materials will be covered with specific examples. Subsequently, the current technology of KNN ceramics and thin films will be presented in terms of strucuture-processing-property relationships. In particular, the major processing methods to fabricate KNN thin films will be intensively introduced from recent publications.

Chapter 3 shows KNN solution preparation, the fabrication of KNN thin films by chemical solution deposition, and the structural and electrical characterization of films by DSC-TG, XRD, Raman spectroscopy, FE-SEM, a ferroelectric tester, and an impedence analyzer.

Chapter 4 and chapter 5 discuss results and their analysis, and summarize the above mentioned chapters.

CHAPTER II

GENERAL BACKGROUND

2.1. Piezoelectricity

Crystals formed by polar molecules with a non-centrosymmetric structure or without a center of symmetry will show a piezoelectric effect. This means that a mechanical stress applied to the crystal will create an overall polarization, and thus creating a voltage across it. The reverse of the stress direction will cause the reverse in the polarity of the polarization and hence the voltage. The piezoelectric effect is convertible. This means that an applied electric field will create a mechanical strain, expansion, or contraction, depending on the direction of the field.

In general, an applied electric field always causes mechanical distortion in the geometric shape of the material, because matter is constructed of charged nuclei surrounded by a compensating electron cloud. The polarization induced by the applied field will cause changes in charge distribution and hence mechanical distortion. The strain resulting from the mechanical distortion is proportional to the square of the field, and this phenomenon, called electrostriction, is not inversive. This means that a mechanical stress action on mass points cannot induce dipole moments from the neutral state of the material. Electrostriction occurs in all materials, although its effect is extremely or negligibly small for most practical cases.

The direct effect of the piezoelectricity is the generation of electric polarization by a mechanical stress acting like a generator, while the inverse effect is the mechanical movement actuated by an electric field acting like a motor. There are two principal mechanisms in piezoelectricity. Based on the first mechanism, the dipole moments may just mutually cancel each other in the material under the unstrained condition. Piezoelectricity may occur if the crystal has no center of symmetry, and in this case the relation between the electric field and the mechanical strain is linear in the first approximation. This linear relationship is sometimes referred to as the linear piezoelectric effect. However, according to the second mechanism, the dipole moment components may remain, but they add to a resulting moment along a polar axis of the unit cell, so the occurance of piezoelctricity is accompanied by pyroelctricity, involving spontaneous polarization. Thus, for ferroelctric piezoelectricity, the variation of the mechanical strain with the applied electric field follows the change of polarization in the hysteresis loop, as shown in Figure 2.1. During the poling process, there is a small expansion of the material along the poling direction and a contraction in directions (lateral directions) perpendicular to it. Therefore, the strain along the poling direction is positive. In Figure 2.1, the solid line traces the poling strain from a virgin state 0 to saturation state C and remanent state D. The lateral strain is negative. Both the poling and the lateral strain-field relations form a butterfly-shaped hysteresis. Figure 2.1 shows the basic differences among electrostriction, linear piezoelectricity, and ferroelectric piezoelectricity.

In general, ferroelectric piezoelectrics, such as ceramics, have advantages for use in transducers because they have a large piezoelectric coefficient, especially near the transition temperature, and a higher dielectric constant that allows the electro-mechanical

coupling factor to approach unity. In comparison with non-ferroelectric materials, ferroelectrics may have a high coupling constant, but they also have high dielectric losses.
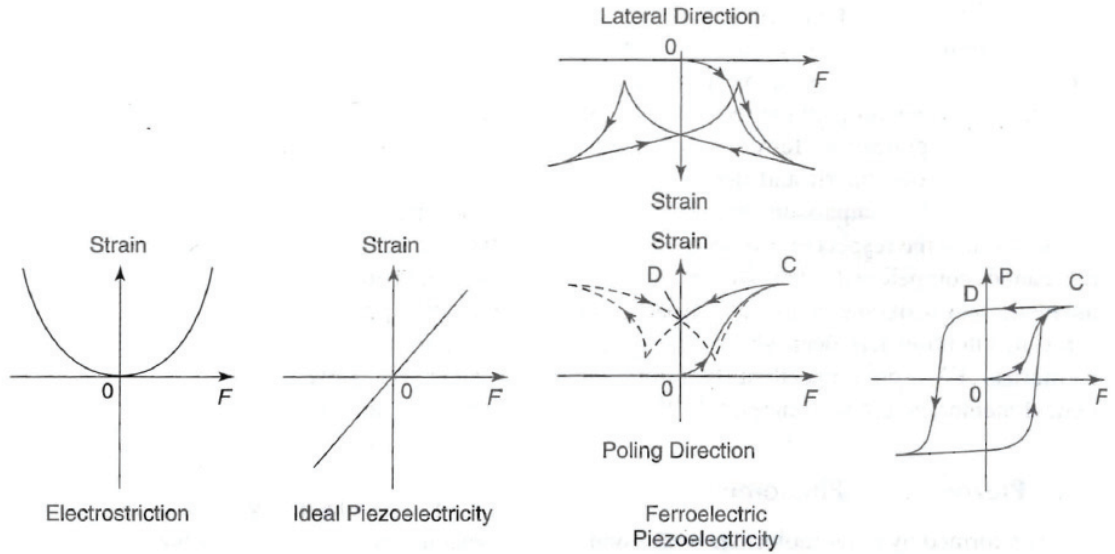
Figure 2.1 Schematic illustration of the variation of mechanical strain with electric field for electrostriction, ideal piezoelectricity, and ferroelectric piezoelectricity in poling and lateral directions [21].

2.1.1. Phenomenological Approach to Piezoelectric Effects

Thermodynamically reversive interactions occur among the electrical, mechanical, and thermal properties, as illustrated in Figure 2.2. The lines joining pairs of circles indicate that a small change in one of the variables causes a corresponding change in the others. The three direct relations are as follows.
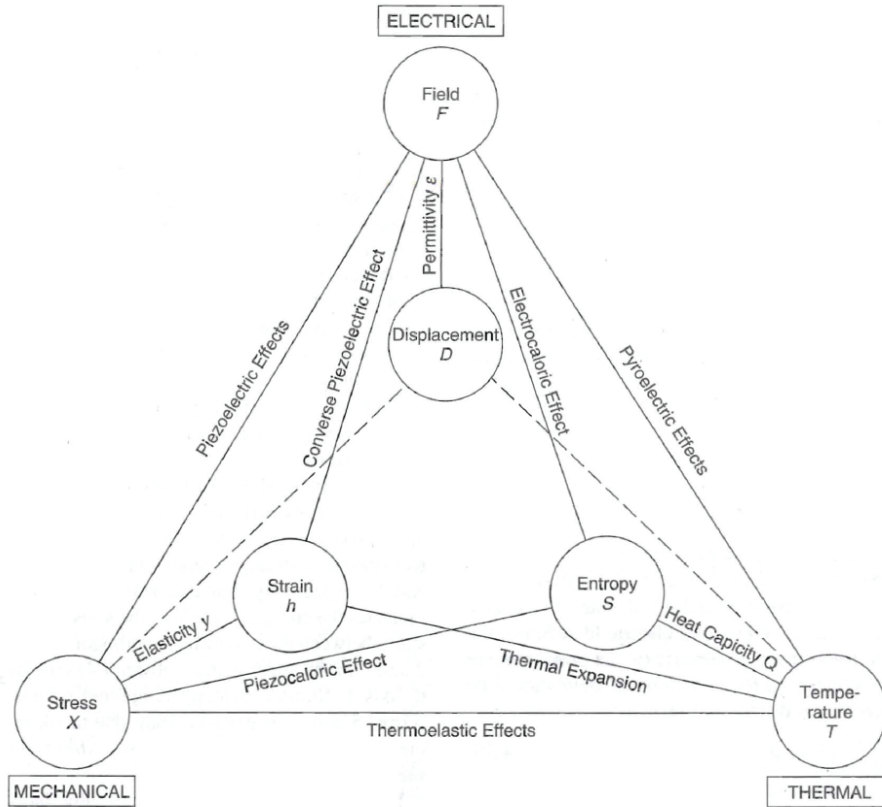
Figure 2.2 The relations between the mechanical, electrical, and thermal properties for crystals with a noncentrosymmetric structure (without a center of symmetry) [21].

The relation between electric field F and displacement D defines the permittivity ε

$$D = \varepsilon F \qquad\qquad \dots\dots \ (1)$$

The relation between mechanical stress X and strain h defines the elastic compliance, or elastic constant y (y=1/Y, where Y is the modulus of elasticity or the elastic stiffness coefficients).

$$h = yX \qquad\qquad\qquad \text{......} (2)$$

The relation between temperature T and entropy S defines the heat capacity Q

$$S = QT^{-1} \qquad\qquad\qquad \text{......} (3)$$

The lines joining the circles at different corners define the coupling effects. For ordinary solids, the properties follow Equations 1 through 3. But for piezoelectric materials, additional terms are required. For example, a mechanical stress causes not only a strain, but also electric polarization, even at a constant temperature. Thus, the displacement induced by the stress can be expressed as

$$D = dX \qquad\qquad\qquad \text{......} (4)$$

where d is one of the pizoelectric constants (or coefficients) whose unit is coulombs/newton.

In the converse piezoelectric effect, we can also express the relation between electric field and the strain as

$$h = dF \qquad\qquad\qquad \text{......} (5)$$

In this case, the unit for d is meters/volt. In fact, for both the piezoelectric and the converse piezoelectric effects, d is identical, therefore

$$d = \frac{D}{X} = \frac{h}{F} \qquad\qquad \text{...... (6)}$$

In terms of the electric field produced by a mechanical stress, the relation becomes

$$F = gX \qquad\qquad \text{...... (7)}$$

In this case, g is another one of the piezoelectric constants. Its unit is [volts/meter]/[newtons/meter^2]. It can be expressed as

$$g = \frac{d}{\varepsilon} = \frac{d}{\varepsilon_r \varepsilon_o} \qquad\qquad \text{...... (8)}$$

There are two other piezoelectric constants, namely e and f, which are only occasionally used. Their relation is

$$X = -eF \qquad\qquad \text{...... (9)}$$

$$F = -fh \qquad\qquad \text{...... (10)}$$

These four piezoelectric constants can be defined in partial derivatives as

$$d = \left(\frac{\partial D}{\partial X} \right)_{F,T}$$

$$g = -\left(\frac{\partial F}{\partial X} \right)_{D,T}$$

9

$$e = \left(\frac{\partial D}{\partial h}\right)_{F,T}$$

$$f = -\left(\frac{\partial F}{\partial h}\right)_{D,T} \qquad (11)$$

Similarly, the piezoelectric constants for the converse piezoelectric effects can be written as

$$d' = \left(\frac{\partial h}{\partial F}\right)_{X,T}$$

$$g' = \left(\frac{\partial h}{\partial D}\right)_{X,T}$$

$$e' = -\left(\frac{\partial X}{\partial F}\right)_{h,T}$$

$$f' = -\left(\frac{\partial X}{\partial D}\right)_{h,T} \qquad (11)$$

Based on the thermodynamic argument, d = d', g = g', e = e', and f = f'.

The interactions between the electrical and the elastic variables describe the piezoelectric effects. The equations of state relating the electrical and the elastic variables can be written in general form as

$$D = dX + \varepsilon^{X} F \qquad \text{...... (12)}$$

$$h = y^{F} X + dF \qquad \text{...... (13)}$$

10

where the superscripts denote the parameters held constant, so ε^X denotes the permittivity at constant stress X and y^F denotes the elastic compliance at constant electric field F. For the ferroelectric piezoelectricity, the properties are nonlinear, so the equations of state should be written in differential form as

$$\delta D = d\delta X + \varepsilon^X \delta F \qquad \qquad \dots\dots (14)$$

$$\delta h = y^F \delta X + d\delta F \qquad \qquad \dots\dots (15)$$

The piezoelectric coefficients are interdependent. For example,

$$\frac{d}{g} = \varepsilon^X$$

$$\frac{e}{f} = \varepsilon^X \qquad \qquad \dots\dots (16)$$

To specify the overall strength of the piezoelectric effect, it is convenient to use the electro-mechanical coupling factor k, which can be considered the direct way to measure the ability of piezoelectric materials to convert one form of energy to another. This coupling factor k is defined as

$$k^2 = \frac{\text{Electrical energy from conversion}}{\text{Total input mechanical energy}} \qquad \qquad \dots\dots (17)$$

resulting from the direct piezoelectric effect, or

$$k^2 = \frac{\text{Mechanical energy from conversion}}{\text{Total input electrical energy}} \qquad \dots\dots \ (18)$$

resulting from the converse piezoelectric effect. Since the electro-mechanical conversion is always incomplete, k is always less than unity. Typical valuues of k are 0.1 for quartz, 0.4 for barium titanate, 0.7 for PZT, and close to 0.9 for Rochelle Salt.

In general, piezoelectric properties are dependent on orientational direction, thus they must be described in terms of tensors. A convenient way to specify the directional properties is to use subscripts that define the direction and orientation, as illustrated in Figure 2.3. The subscript 3 refers to the polar axis (or poling axis); 1 and 2 refer to arbitrarily chosen orthogonal axes perpendicular to 3. Subscripts 4, 5, and 6 refer the shear planes of the mechanical stress and strain perpendicular to axes 1, 2, and 3, respectively. For example, subscript 4 indicates the change of angle of the stress, or the strain between the two initially orthogonal axes 2 and 3 in the shear plane (subscript 4) normal to axis 1. Similar meaning is applied to subscripts 5 and 6. Stress and strain due to shearing action are referred to as the shear stress and shear strain.

Piezoelectric coefficients are usually indicated with two subscripts denoting the direction of the properties. The first subscript refers to the direction of the electric field F (or the displacement D). The second subscript refers to the direction of the mechanical stress X (or the strain h). For example, in the case of d_{31}, the second subscript 1 refers to

12

the stress or strain direction normal to the field direction, whereas for d_{33}, the second

subscript 3 refers to the stress or strain direction parallel to the field direction.
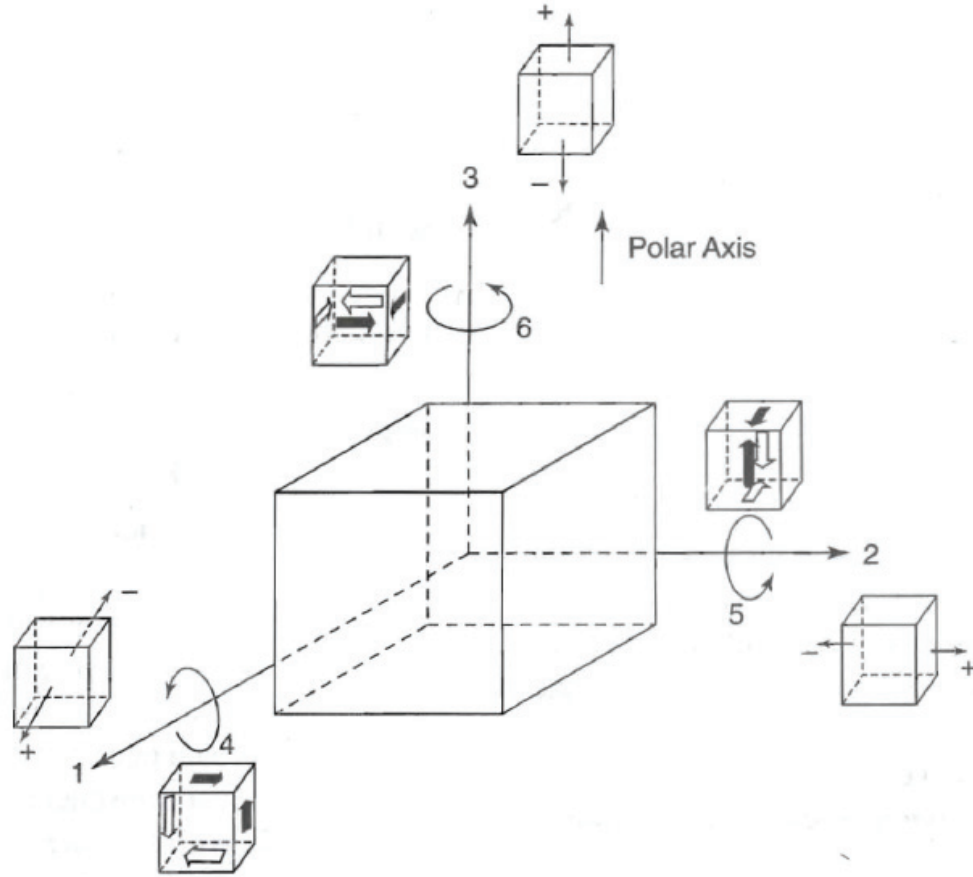
Figure 2.3 Subscript symbols for the notation of the directional properties for poled

piezoelectric materials [21].

In most cases, it can be assumed that the plane perpendicular to the polar axis is

isotropic. This implies that an electric field pararell to polar axis 3 interacts in the same

way, with the mechanical stress either along axis 1 or along axis 2. Thus, $d_{31} = d_{32}$, $d_{15} =$

d_{24}, $y_{13} = y_{23}$, etc. It should be noted that shear can only occur when an electric field is

applied at right angle to the polar axis, so there is only one shear piezoelectric coefficient

d_{15} (since $d_{15} = d_{24}$). There are also piezoelectric coefficients corresponding to hydrostatic stress. In this case, $d_h = d_{33} + d_{31} + d_{32} = d_{33} + 2d_{31}$. Similar notations are used for other piezoelectric coefficients, such as g_{33}, g_{31}, g_{15}, g_h, etc.

Elastic properties can also be specified in terms of elastic compliance y, such as y_{11}, y_{12}, y_{13}, y_{33}, y_{44}, y_{66}, to denote the interaction of a strain and a stress under the condition of constant field. Thus y should be written as y_{11}^F, y_{12}^F, y_{13}^F, y_{33}^F, y_{44}^F, y_{66}^F (usually for F = 0). Each y relates to the application of a single stress in one direction; the other ys are kept fixed so that there is no lateral restraint. Stress and strain are interchangeable, so $y_{13} = y_{31}$. The permittivity ε should also be a tensor, but for most cases, the field has only one direction, oblique components being negligible, so one subscript is sufficient. For example, $\varepsilon_{33} = \varepsilon_3$, $\varepsilon_{31} = \varepsilon_1$, $\varepsilon_{32} = \varepsilon_2$, etc. indicating that ε_3 is the permittivity along the polar axis 3, and ε_1 and ε_2 are the permittivities along axes 1 and 2, respectively.

2.1.2. Piezoelectric Materials

The most important piezoelectric materials are the ceramics consisting of crystallites of perovskite structure, such as PZT and PLZT; the synthetic polymers, such as PVDF; and the ceramic-polymer composites. Table 2.1 lists the typical values of some important parameters of some commonly used piezoelectric materials. All ferroelectric materials are piezoelectric, but not all piezoelectric materials are ferroelectric. From now on some special features of several piezoelectric materials will be described.

Table 2.1 Selected properties of some piezoelectric materials: d = piezoelectric constant, k = electro-mechanical coupling factor, and ρ= density [21].

Material (Abbreviation)	Chemical Formula	d (cm V^{-1})	k	ρ (g cm^{-3})
Silicon Dioxide (Quartz)	SiO_2	2.25×10^{-10}	0.099	2.65
Potassium-Sodium Tartrate-Tetrahydrate (Rochelle Salt)	$KNaC_4H_4O_6 \cdot 4H_2O$	5.30×10^{-9}	0.78	1.77
Barium Titanate	$BaTiO_3$	1.90×10^{-8}	0.38	5.70
Ammonium Dihydrogen Phosphate (ADP)	AH_2PO_4	2.46×10^{-9}	0.29	1.80
Potassium Dihydrogen Phosphate (KDP)	KH_2PO_4	1.07×10^{-9}	0.12	2.31
Triglycine Sulfate (TGS)	$(NH_2CH_2COOH)_3 \cdot H_2SO_4$	5.00×10^{-9}	—	1.69
Potassium Niobate or Sodium Niobate	$KNbO_3$ or $NaNbO_3$	4.90×10^{-9}	0.42	4.45
Lithium Niobate	$LiNbO_3$	0.85×10^{-10}	0.035	4.64
Lithium Tantalate (LT)	$LiTaO_3$	3.00×10^{-10}	0.10	7.46
Lead Titanate	$PbTiO_3$	7.40×10^{-10}	—	7.12
Lead Zirconate Titanate (PZT)	$Pb(Zr_{1-x}Ti_x)O_3$	2.34×10^{-8}	0.66	7.70
Polyvinyl Chloride (PVC)	see Table 5-2	0.70×10^{-10}	—	1.40
Polyvinyl Fluoride (PVF)	see Table 5-2	1.00×10^{-10}	0.03	—
Polyvinylidene Fluoride (PVDF or Kynar)	see Table 5-2	4.00×10^{-10}	0.12	1.78

Quartz is a commonly used piezoelectric crystal, but crystals of the water-soluble type have a much larger electromechanical coupling factor k. For example, ammonium dihydrogen phosphate (ADP) has k ≈ 0.30. Still higher coupling can be achieved with ferroelectrics such as PZT (a $PbTiO_3$ and $PbZrO_3$ mixture). The PZT specimen, after being poled with a sufficiently strong electric field, exhibits high values of k_p and d depending on the composition, as shown in Figure 2.4. Aliovalent substituents would modify the properties of ceramics with a perovskite structure. In order to achieve a given

set of properties, PZT-based ceramics may require composition of more than one type of additive.
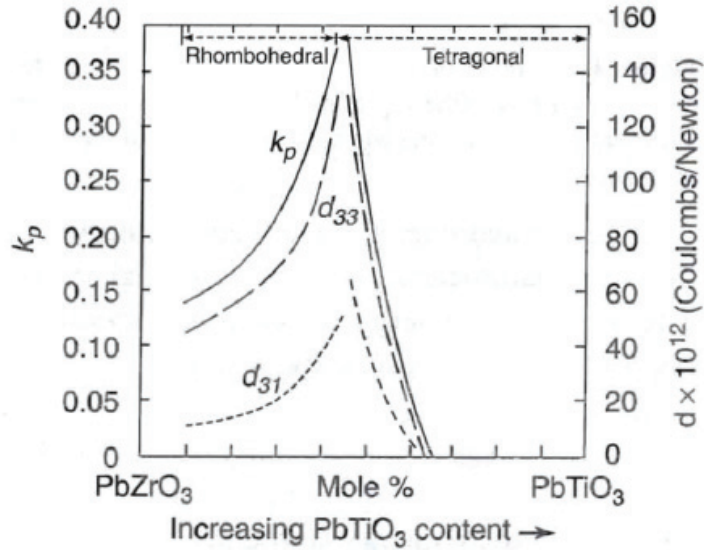
Figure 2.4 The planar electromechanical coupling factor k_p and piezoelectric coefficient d as functions of the composition of the PZT ceramics [21].

One system that has been widely used for piezoelectric devices is PZT doped with lanthanum to form a new PLZT system. Such systems usually contain 3 - 12 mol% La and 5 - 30 mol% Ti. For the system with the composition of La : Zr : Ti = 7 : 60 : 40, the values of k_p and d_{33} have reached 0.72 and 7.1×10^{-10} m/V [22 - 23]. Such high values of k_p and d_{33} have been attributed to the compositions located within the boundary region between the rhombohedral and tetragonal phases [24 - 25]. PLZT may also contain vacancies on B (as well as on A) sites, providing a favorable way to change their polar states under the influence of applied fields.

Polymer films have the following advantages: they are flexible and tough, they can be made very thin (< 10 μm) and large in area, they can be shaped into any geometric

16

forms, and they have a low mechanical impedance. Polymers, particularly PVDF, have been used widely for various transducers and sensors. For PVDF, the piezoelectric coefficient d and the pyroelectric coefficient p are closely related to the poling parameters. They increase linealy with increasing poling field F_p, poling temperature T_p, and poling time t_p, as shown in Figure 2.5. The data are from Murayama et al. [26 - 27].
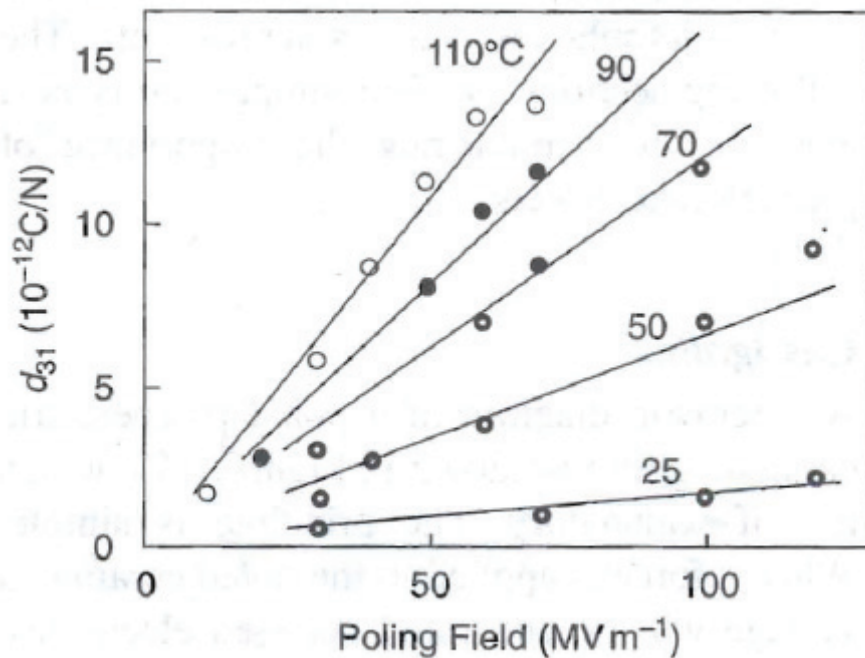
Figure 2.5 The piezoelectric coefficient d_{31} of PVDF at room temperature as a function of poling field and poling temperature for the fixed poling time of 30 minutes [26].

Apart from PVDF, other polymers, such as polyvinyl fluoride (PVF), polyvinyl chloride (PVC), and PTFE, also exhibit piezoelectric effects. PVC is a noncrystalline polymer but has relatively high piezoelectric and pyroelectric coefficients when poled at

high temperatures. It should be noted that the properties of polymers depend strongly on the preparation techniques and conditions.

To produce materials with optimal properties for a special application, we may choose a suitable ceramic-polymer composite. In general, a composite refers to a mixture in which ferroelectric ceramic particles are dispersed in a polymer matrix. The properties are largely determined by the choice of components, their relative composition, and the manner in which they are interconnected. The composites made by mixing PZT ceramic, PVDF polymer, and fluorinated rubber have a good piezoelectric coefficient, depending on the composition [28]. Ceramic-polymer composites have been developed mainly to search for a suitable combination that can be adapted for piezoelectric or pyroelectric devices to be used in stringent environments, such as sonar devices in water and sensors for medical diagnostics.

2.1.3. Applications of Piezoelectrics

Both the direct and converse piezoelectric effects can be used for many practical applications, such as high-voltage generators, cigarrette lighters, gas igniters, transducers for high intensity ultrasounds employed in ultrasonic cleaning, ultrasonic therapy, medical diagnosis, and delay lines, resonators for filters, oscillators, microphones, and various sensors. The following sections use four simple and typical examples to demonstrate the importance of piezoelectric effects.

2.1.3.1. Gas Igniters

A schematic diagram of a poled piezoelectric ceramic igniter is shown in Figure 2.6. When a force is applied to the poled ceramic, a voltage will be generated between electrodes. It is usual to use two pieces of poled ceramic elements connected back to back
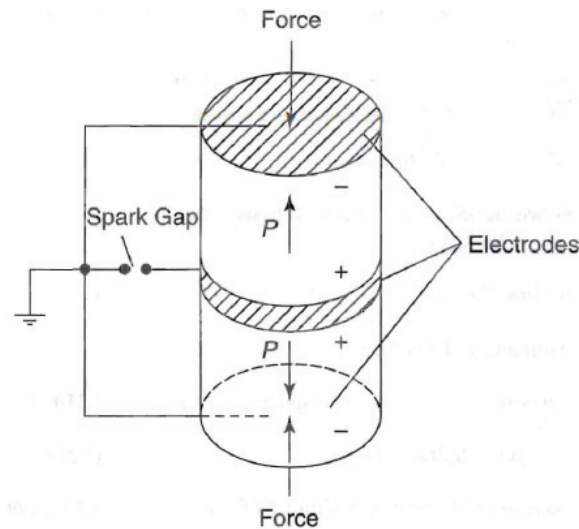
Figrure 2.6. Schematic diagram illustrating the principle of a gas igniter [21].

in order to double the charges released for the spark. On releasing the force, a voltage of about the same magnitude, but of the opposite sign, will be produced, yielding another spark across the gas gap. If the force were applied too slowly, no spark would occur because the charges released gradually would leak away through the leakage across the electrode, instead of building up to generate a high voltage across the spark gap. This is why igniters are of the momentary impact type rather that the slow squeeze type.

Since most igniters have two pieces of poled ceramic elements connected back to back, we need consider only one for our analysis. Based on Equation 7, the voltage developed across the ceramic element when an impact force is applied is given by

19

$$V = F\ell = g_{33}\ell X = g_{33}\ell\frac{F}{A} \quad \ldots\ldots (19)$$

where F is the force and ℓ and A are, respectively, the length and the area of the ceramic element. Ignoring all possible losses in the operation, the energy that may be dissipated in the spark is

$$W = \frac{1}{2}\varepsilon_{33}\frac{A}{\ell}\left(g_{33}\ell\frac{F}{A}\right)^2 = \frac{1}{2}d_{33}g_{33}\frac{F^2\ell}{A} \quad \ldots\ldots (20)$$

If two elements are connected back to back (in fact, they are connected in parallel), the total energy available for the spark is two times that shown in Equation 20. PZT and PLZT are commonly used for gas igniters.

2.1.3.2. Delay Lines

The transmission of a microwave signal can be delayed by the following step:

1. The microwave signal is guided through a coupling network to a piezoelectric transducer, which converts it to an acoustic wave.

2. This acoustic wave then propagates in a dielectric medium and reflects when it reaches the end.

3. This reflected acoustic wave will be converted back to the original microwave signal by the transducer, as shown in Figure 2.7.

The major advantage of this type of delay line is the use of the transducer to convert the high-speed microwave signal to a low-speed acoustic wave, and of the dielectric medium to produce the time delay. Since the speed of an acoustic wave is about 10^5 times slower than an electromagnetic wave, this type of delay line can be made much smaller in size and weight than a conventional one.
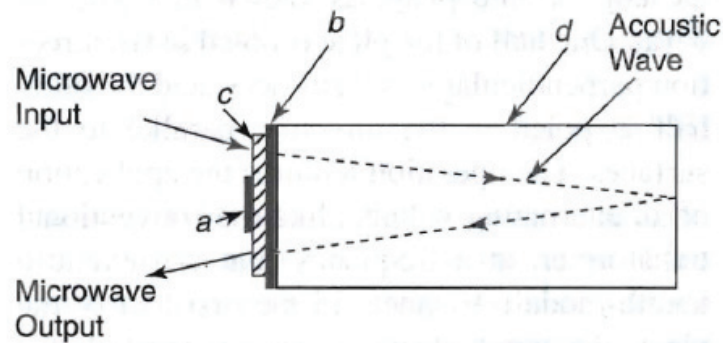
Figure 2.7 The structure of a microwave delay line; a: electrode A, b: electrode B, c: transducer, and d: dielectric medium [21].

2.1.3.3. Piezoelectric Positioners and Actuators

Piezoelectric positioners and actuators have been used widely in areas related to precision position controlling, vibration damping, relays, phonograp pickup, and pressure sensing [29-31].

The basic principle is simple. A thin piezoelectric plate with metallic electrodes deposited on both surfaces can be used as a mechanical positioner or relay when the required movements are very small (e.g., a few micrometers or less).

Figure 2.8 shows schematically a poled rectangular piezoelectric plate with the following dimensions: length a, width b, and thickness c, which are in the x, y, and z directions, respectively. When a DC voltage V is applied across the thickness in the z direction which is also the poled direction, then the plate will expand or contract in the z direction, and contract or expand in the x and y directions, depending on the polarity of the voltage with respect to the poled direction. The magnitude of such movements can be easily calculated. From Equation 6, we can write

$$d_{33} = \frac{h}{F} = \frac{\Delta c / c}{V / c} = \frac{\Delta c}{V}$$

or

$$\Delta c = d_{33} V \qquad\qquad (21)$$

This indicates that the change in thickness (i.e., the movement) depends on the piezoelectric coefficient d_{33} and the applied voltage V, but is independent of the thickness.
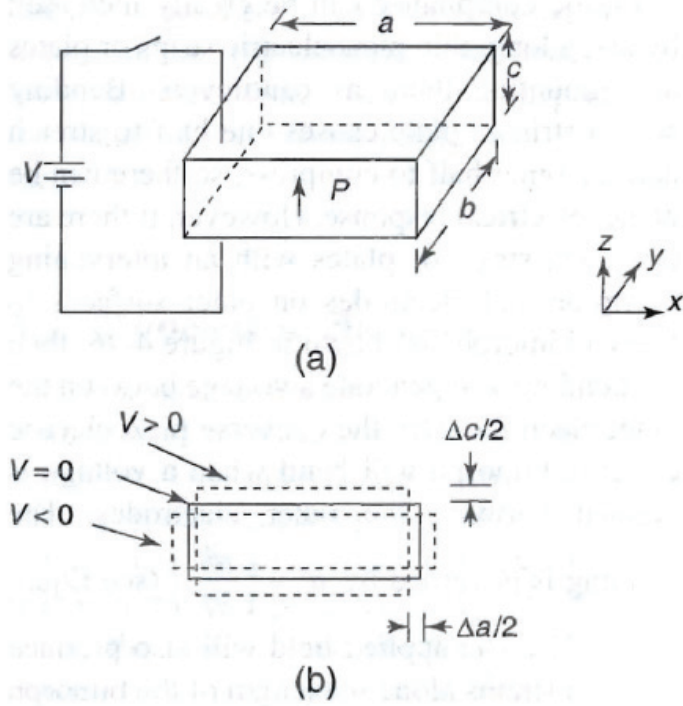
Figure 2.8 Schematic illustration of the deformation of a poled piezoelectric plate under an electric field: (a) the original shape of the plate at $V = 0$ and (b) the deformation at $V > 0$ and $V < 0$ (The deformation is exaggerated for clarity.) [21].

For movements in the direction normal to the poled direction (for example, in the x direction), we have

$$d_{31} = \frac{h}{F} = \frac{\Delta a / a}{V / c} = \left(\frac{c}{a}\right)\frac{\Delta a}{V}$$

$$\Delta a = \left(\frac{c}{a}\right)d_{31}V \qquad (22)$$

It can be seen that in this case, a can be made much larger than c if a >> c. For a very small adjustment in the position, we may use a small and more precise movement in the direction parallel to the poled direction. But for a larger movement, such as for relays, sideways movement in the direction normal to the poled direction may be preferable.

Elastic compliance can be greatly increased by using long, thin piezoelectric strips or plates and mounting them as cantilevers. Bending such a strip or plate causes one half to stretch and the other half to compress, so there can be no net electrical response. However, if there are two such strips or plates with an intervening electrode and electrodes on outer surfaces to form a bimorph, as shown in Figure 2.9, then the bending will generate a voltage between the outer electrodes.
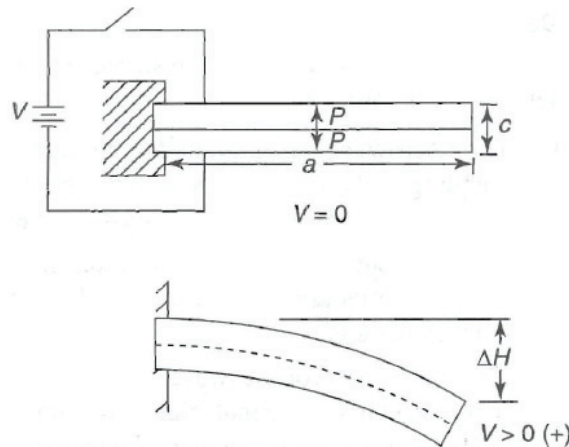
Figure 2.9 Schematic illustration of the bending of a bimorph cantilever-piezoelectric actuator (The bending magnitude is highly exaggerated for clarity.) [21].

By the converse piezoelectric effect, a bimorph will bend when a voltage is applied between the outer electrodes. The bending is governed by $d' = \left(\dfrac{\partial h}{\partial F}\right)$ as shown in Equation 11. The applied field will also produce uniform strains along the length of the bimorph so that it will be in the form of a circular arc. Detailed analysis of the behavior of the bimorph under static conditions has been done by several investigators [32-33]. The reflection at the free end of the bimorph cantilever is given by

$$\Delta H = \frac{3}{2}\left(\frac{a^2}{c^2}\right)d_{31}V \qquad (23)$$

In this case, ΔH is proportional to $(a/c)^2$. This is why bending actuators are widely used for the applications requiring large movements, because they provide the largest movement (deflections) for a given applied voltage. It should be noted that bending bimorphs are not suitable for some applications because they have high mechanical inertia and cannot produce significant forces.

The basic principle is simple. A thin piezoelectric plate with metallic electrodes deposited on both surfaces can be used as a mechanical positioner or relay when the required movements are very small

2.1.3.4. Piezoelectric Transformers

A transformer can be formed simply by a piezoelectric plate with electrodes deposited on half of its two flat surfaces and an electrode on the edge of the plate, as shown in
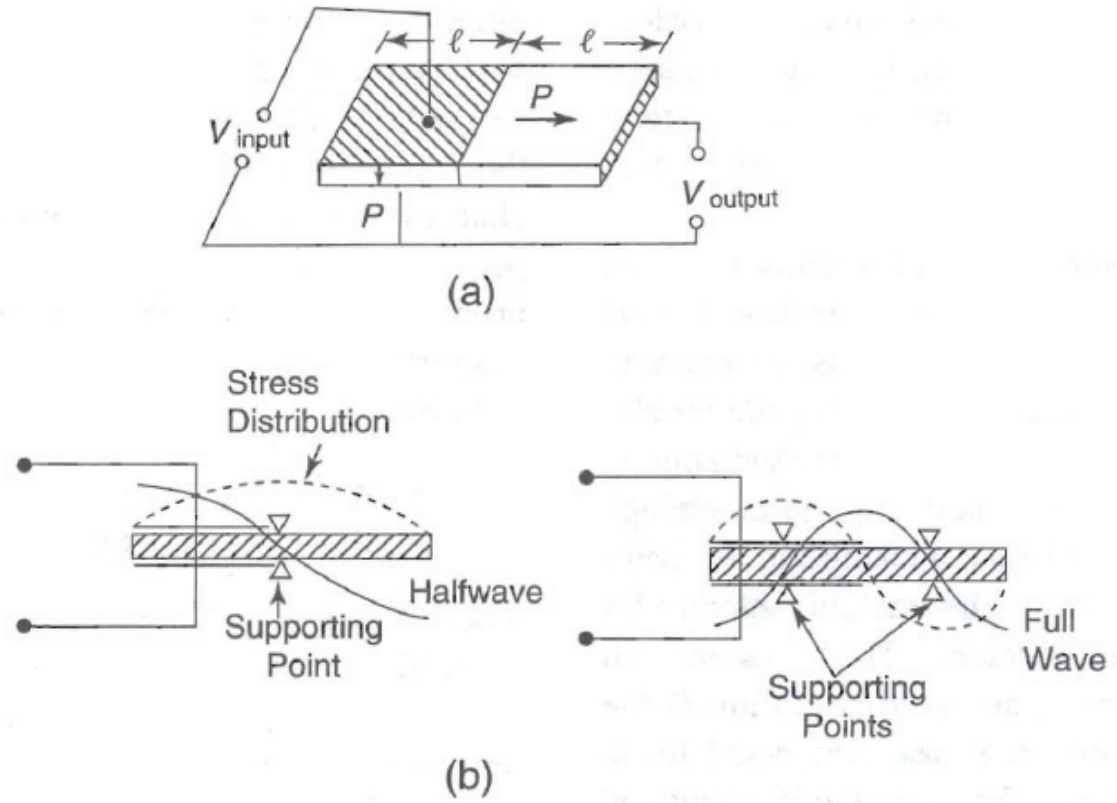
Figure 2.10 (a) Schematic illustration of a piezoelectric transformer and (b) the half- and full-wave resonances [21].

Figure 2.10(a). One half of the plate is poled in the directions perpendicular to the surfaces, and the other half is poled in the direction parallel to the surfaces. The operation requires the application of an alternating voltage, like the conventional transformer, at a frequency that can excite a length-mode resonance. In the first half of the plate, the input electrical energy through the input terminal is converted into mechanical energy, which results in oscillatory vibration. This mechanical energy is then converted back to electrical energy and picked up at the output terminal. It is important that the length of the plate be equal to a number of half-wavelengths of the acoustic wave to allow standing

waves to form. In short, the mechanical oscillations in the first part are transmitted at resonance to the second part, which reconverts the mechanical energy into electrical energy, resulting in the generation of a higher voltage. The resonant frequency is determined by the acoustic velocity v in the piezoelectric material. If the total length of the transformer is 2ℓ, then for the transformer length equal to one full wavelength, the full wave resonant frequency is

$$f = \frac{v}{2\ell} \qquad (24)$$

For the transformer length equal to a half wavelength, the half-wave resonant frequency is

$$f = \frac{v}{4\ell} \qquad (25)$$

Figure 2.10(b) shows that half-wave and the full-wave resonance. Since the operation of the transformer is based mainly on the resonance conditions, the location of the supporting points in the installation of such transformers is very important. In general, supporting points must be located at places where the oscillatory vibration is zero, as shown in Figure 2.10(b).

2.2. Non-lead $(K_xNa_x)NbO_3$ (KNN) Piezoelectric Materials

2.2.1. KNN Ceramics and Piezoelectric Properties

The phase diagram for the solid solution $(1-x)KNbO_3-(x)NaNbO_3$ system is given in Figure 2.11. Reported in 1955, a morphotropic phase boundary (MPB) was identified at $x \sim 0.5$ separating two orthorhombic ferroelectric phases. Inherent to MPBs, a maximum in remnant polarization (P_r) and minimum in coercive field (E_c) were reported [34]. A broad maximum in the planar coupling coefficient was observed, however, with no enhancement in the dielectric properties for either air-fired or hot pressed materials as shown in Figure 2.11(b). Table 2.2 presents dielectric and piezoelectric data for KNN with MPB compositions, reported prior to 1962 and for material recently processed using "optimal" processing and various fluxes. As presented, no significant differences in the piezoelectric properties are observed.

a

b
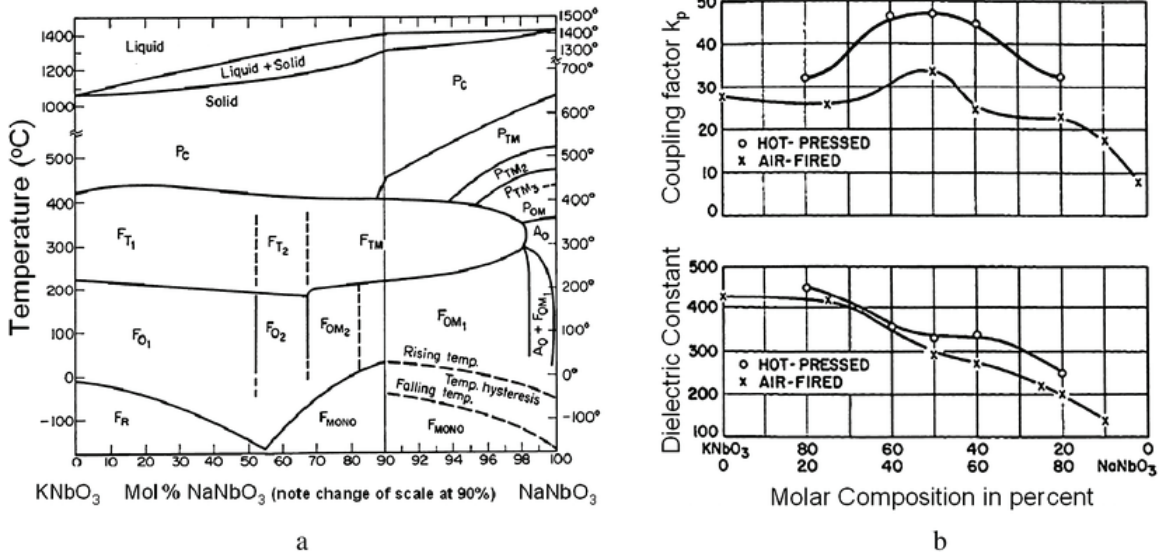
Figure 2.11 (**a**) Phase diagram for the KNbO$_3$-NaNbO$_3$ system [35] and (**b**) dielectric and piezoelectric properties as a function of composition [34] Note: the orthorhombic–orthorhombic MPB is at ～50 mol% NaNbO$_3$

Table 2.2 Dielectric and piezoelectric properties of KNN ceramics: "past" and "present" [36].

Properties	Air–fired 1959 [47]	Hot Pressed 1962 [45]	Standard 2005–2006 [16, 48, 52]	CuO flux 2005 [16]	KCT/KCN Flux 2005 [17, 18]	ZnO Flux 2006 [52, 54]
ε_r	290	490	429–605	231	250	500–650
d_{33} (pC/N)^a	80	127	98–107	86	90(High Field-190)	117–123
k_p	36%	~46%	33.4–40%	37.8%	41%	0.4–0.44

It is important to note, KNN material prepared by spark plasma sintering reported significantly higher dielectric and piezoelectric properties than those given in Table 2.2, with ε_r～700 and d_{33}～148 pC/N [37-38]. It is suggested that the enhancement is the result of extrinsic contributions to the polarizability associated with submicron grain sizes, similar to that found in fine grain BaTiO$_3$ [39].

For the KNN family, reports of enhanced dielectric and piezoelectric properties were attributed to a morphotropic phase boundary separating orthorhombic and tetragonal phases [40-46]. Though technically a MPB, the enhancement in properties is a result of compositionally shifting the $T_{\text{O–T}}$ polymorphic phase transition downward to room temperature. As first reported in BaTiO$_3$ [47], and later in KNbO$_3$ [47], the enhanced polarizability associated with a polymorphic phase transition leads to maxima in the dielectric and piezoelectric properties. This behavior is clearly shown for the case of Cd modified NaNbO$_3$ [47] and pure KNbO$_3$ [47] in Figures 2.12 and 2.13, respectively. As

shown, maxima occurred at all the ferroelectric–ferroelectric polymorphic phase transitions, with the highest levels of piezoelectric activity belonging to the orthorhombic-tetragonal transition.
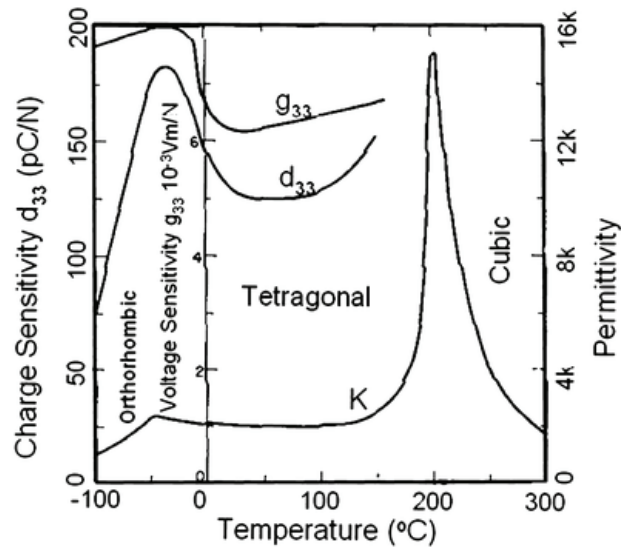
Figure 2.12 Dielectric constant and piezoelectric coefficient versus temperature for $Na_{0.75}Cd_{0.125}NbO_3$ [47].
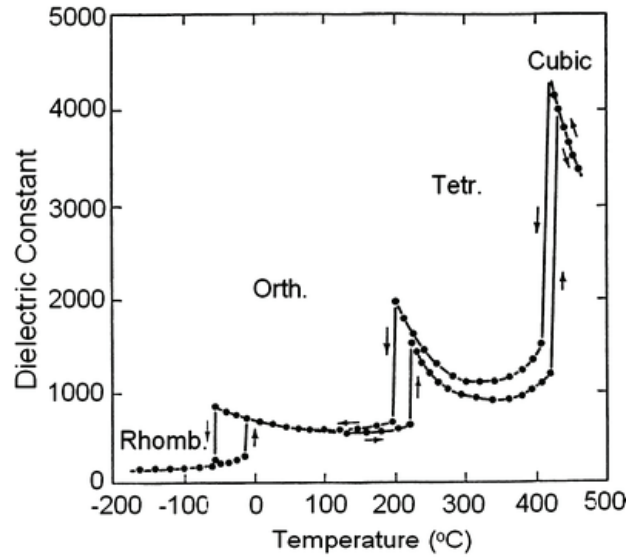
Figure 2.13 Dielectric constant versus temperature for KNbO$_3$, showing the various polymorphic phase transitions [47].

Figure 2.14 gives the dielectric permittivity and dielectric loss for a modified KNN over the temperature range of -50 – 450 °C. As shown, two dielectric anomalies are presented with the $T_c \sim 380$°C belonging to the tetragonal-cubic phase transition and the anomaly at room temperature being associated with the orthorhombic–tetragonal (T_{O-T}) polymorphic phase transition. The enhancement in piezoelectricity is clearly evident in Figure 2.15, where maxima in both coupling coefficient and piezoelectric d_{31} are again found at the T_{O-T} for two representative KNN compositions.
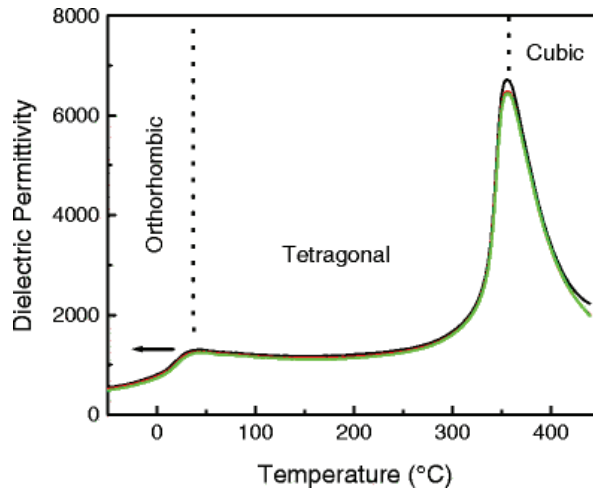
Figure 2.14 Dielectric permittivity as a function of temperature for a KNN-LS5% material [48].
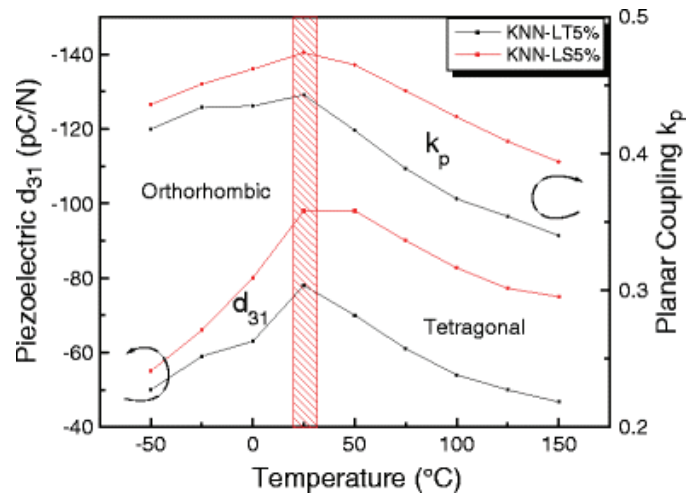
Figure 2.15 Piezoelectric coefficient and coupling factor as a function of temperature for LiTaO$_3$ (LT) and LiSbO$_3$ (LS) modified KNN systems [48].

Figure 2.16 presents the phase diagram of the KNN system as a function of compositional modifications, including LiTaO$_3$, LiNbO$_3$, and SrTiO$_3$ [49-52], in which

T_{O-T} can be readily shifted from ~200 °C for pure KNN to room temperature with ~5 mol% additions. Similar phase diagrams and their compositional temperature dependence on the various polymorphic phase transitions are well documented for $KNbO_3$-$KTaO_3$ [47] and $BaTiO_3$ [47], the latter being the underlying basis for the development of temperature stable ceramic capacitors.
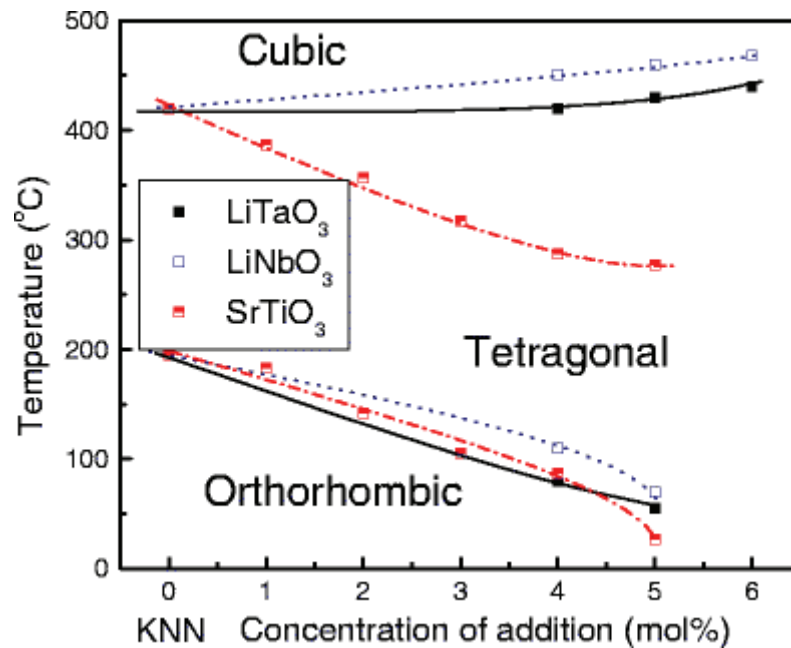
Figure 2.16 Phase diagram for modified KNN [49-52] Note: $BaTiO_3$ additions are analogous to $SrTiO_3$ [50].

From the above, it is evident that the temperature dependence of a polymorphic ferroelectric–ferroelectric phase transition mimics the compositional dependence of properties for a true MPB.

Presented in Figure 2.17, a maximum in P_r is evident at the T_{O-T} polymorphic phase transition near room temperature, analogous to a MPB composition. This maximum in P_r is expected owing to the summation of possible crystallographic orientations, with 12 [110] spontaneous polarization directions for an orthorhombic phase and 6 [001] directions for a tetragonal phase. However, at this time, it is difficult to explain the maximum in E_C, which generally reaches a minimum near a MPB. The decrease of E_C with increasing temperature can be explained by the fact that the domain wall motion and polarization reversal becomes easier with increasing temperature, a thermally activated process.
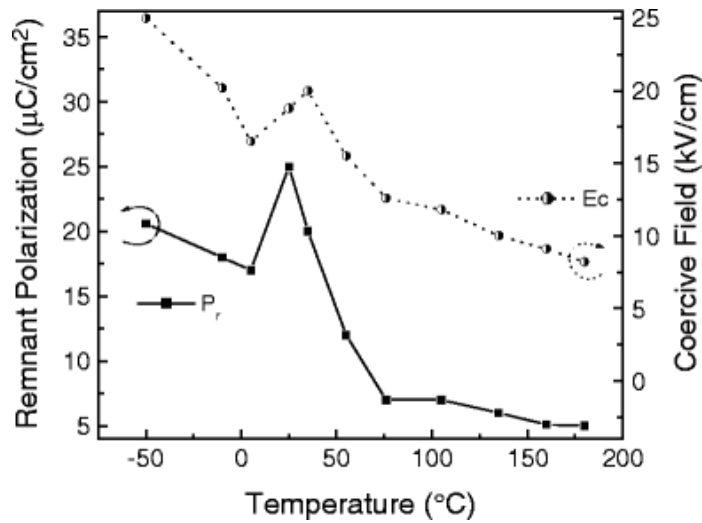
Figure 2.17 Remnant polarization and coercive field as a function of temperature for KNN-LS [53].

2.2.2. KNN Thin Film Deposition and Piezoelectric Properties

2.2.2.1. Chemical Solution Deposition (CSD)

A non-vacuum deposition technique, namely, the chemical solution deposition (CSD)

method has been widely investigated for thin film growth for nearly two decades and much of these activities have been aimed at ferroelectric thin films for electronic applications [54-57]. These materials are integrated with silicon technology for ferroelectric memory applications [58], where a (111) texture is desired, and as well as for pyroelectric and microelectromechanical systems (MEMS) applications. There are further growing applications in other areas like thin films for superconductors, optical and magnetic devices, electrochemistry, nanotechnology, protective and decorative coatings and catalysis. The main advantages of the CSD route over physical vapor deposition (PVD) are: (a) it is easy to control the composition of such compounds by changing the stoichiometric ratio of the starting material to ensure high homogeneity, (b) it has a relatively low processing temperature and it does not take a longer time to prepare as compared to solid state reactions, and (c) it is cost effective. This method also has the advantage of quick prototyping so that a large number of film compositions can be quickly tested in a cost-effective manner.

The general principle involved in the solution deposition is to prepare a homogeneous solution of the necessary cation species that may later be applied to a substrate. The fabrication of thin films by this approach involves four basic steps: (i) synthesis of the precursor solution, (ii) deposition by spin coating, spraying, dip-coating or slot die coating, where drying processes usually begin depending on the solvent, (iii) low-temperature heat treatment for drying, pyrolysis of organic species (typically 300 - 400 $^{\circ}$C), and formation of an amorphous film, and (iv) higher-temperature heat treatment (600 - 1100 $^{\circ}$C) for densification and crystallization of the coating into the desired oxide phase. For most solution deposition approaches, the final three steps are similar despite

differences in the characteristics of the precursor solution, and for electronic devices, spin coating has been used almost exclusively. Depending upon the solution route employed, different deposition and thermal processing conditions may be employed to control film densification and crystallization for the preparation of materials with optimized properties. The selection of the starting reagents is dictated by solubility and reactivity considerations and the type of solution precursor species desired. In addition to precursor characteristics, film processing behaviour, such as substrate wetting, can also play a role in determining the solution chemistry that must be developed. Film properties that can necessitate changes in solution chemistry include poor thickness uniformity (striations), crack formation, crystallization behaviour and lack of phase purity, and compositional non-uniformities [59].

Currently, there are a few reports of structural and electrical properties of KNN thin films fabricated by CSD. Kiyotaka Tanaka *et al*. showed that highly oriented single-phase KNN thin films on SiO_2/Si substrates were obtained at 500 °C by spin-coating technique. At temperature lower than 600 °C, volatilization of alkaline elements seemed to have been suppressible [18]. Also, the $K_{0.52}Na_{0.58}NbO_3$ thin film showed a low leakage current density (10^{-7} A/cm^2 at 40 kV/cm), and the maximum polarization P_{max} and dielectric constant ε_r at 1 kHz were 9.1 µC/cm^2 and 725, respectively [17]. To compensate the volatilization of alkaline elements, Yoshifumi Nakashima et al. fabricated KNN thin films prepared from the solution with $K_{0.55}Na_{0.55}NbO_3$ composition showed reasonable ferroelectric P-E hysteresis loops and field-induced strain loops. The $2P_r$ and $2E_c$ values of the $K_{0.55}Na_{0.55}NbO_3$ films were 14 mC/cm^2 and 140 kV/cm, respectively. Also, the effective d_{33} was found to be 46 pm/V [19-20].

2.2.2.2. Pulsed Laser Deposition (PLD)

Laser was first demonstrated in 1960. Since then it has been developed into a powerful tool in many applications. It is especially useful in material processing. Laser possesses many unique properties such as narrow frequency bandwidth, coherence and high power density. Often the light beam is intense enough to vaporize the hardest and most heat resistant materials. Besides, due to its high precision, reliability and spatial resolution, it is widely used in the industry for machining of thin films, modification of materials, material surface heat treatment, welding and micro patterning. Apart from these, polycomponent materials can be ablated and deposited onto substrates to form stoichiometric thin films. This last mentioned application of laser is the so-called pulsed laser deposition (PLD).

In general, the idea of PLD is simple. A pulsed laser beam is focused onto the surface of a solid target. The strong absorption of the electromagnetic radiation by the solid surface leads to rapid evaporation of the target materials. The evaporated materials consist of highly excited and ionized species. They presented themselves as a glowing plasma plume immediately in front of the target surface if the ablation is carried out in vacuum.

Indeed, PLD is so straightforward that only a few parameters, such as laser energy density and pulse repetition rate, need to be controlled during the process. The targets used in PLD are small compared with the large size required for other sputtering techniques. It is quite easy to produce multi-layered films of different materials by sequential ablation of assorted targets. Besides, by controlling the number of pulses, a fine control of film thickness down to atomic monolayer can be achieved. The most

important feature of PLD is that the stoichiometry of the target can be retained in the deposited films. This is the result of the extremely high heating rate of the target surface (10^8 K/s) due to pulsed laser irradiation. It leads to the congruent evaporation of the target irrespective of the evaporating point of the constituent elements or compounds of the target. And because of the high heating rate of the ablated materials, laser deposition of crystalline film demands a much lower substrate temperature than other film growth techniques. For this reason the semiconductor and the underlying integrated circuit can refrain from thermal degradation.

High-quality $(K,Na)NbO_3$ thin films were successfully deposited on a (100) $SrTiO_3$ (STO) substrate by pulsed laser deposition [60]. High-density $KNbO_3$ (KN), $(K_{0.5}Na_{0.5})NbO_3$ (KNN) and $NaNbO_3$ (NN) ceramic targets were prepared by spark plasma sintering (SPS). The crystallographic analyses of the film were performed by conventional X-ray diffraction (XRD) analysis and rocking curve measurement. The XRD reciprocal space map was also measured to determine the lattice constants of the film and analyze the crystallographic relationship between the grown film and the STO substrate.

High-quality $NaNbO_3$ (NN) thin films were epitaxially grown on a (100)$SrTiO_3$ substrate by pulsed-laser deposition [61]. In order to characterize their dielectric properties, the NN films were epitaxially grown on (100)$SrRuO_3$ // (100)$SrTiO_3$ substrates. The relative dielectric constant, ε_r, and dielectric loss, tan δ of the film were 252 and 0.03 at 1 kHz, respectively. When the temperature dependence of ε_r was measured, ε_r was found to suddenly increase at 377 °C, which corresponds to the

transition temperature of NN between the antiferroelectric and paraelectric phases. The P-E hysteresis loop of the NN films exhibited characteristic ferroelectric behavior.

Ambient oxygen pressure in a pulsed laser deposition process has been observed to have a critical influence on the compositional, crystalline, and electrical properties of $Na_{0.5}K_{0.5}NbO_3$ (NKN) thin films grown onto polycrystalline $Pt_{80}Ir_{20}$ and SiO_2(native oxide)/Si(111) substrates [8]. Films prepared at *high oxygen pressure* (~400 mTorr) were found to be single phase and highly *c*-axis oriented. X-ray diffraction θ–2θ scans and rocking curve data show a strong effect of NKN film *self-assembling* along the [001] direction regardless of the substrate texture. The high dielectric permittivity of 550, low dissipation factor of less than 3%, and high remanent polarization of 12 $\mu C/cm^2$ indicate the high ferroelectric quality of the fabricated film. On the other hand, films grown at *low oxygen pressure* ($\sim$ 10 mTorr) have been found to be mixed phases of ferroelectric NKN and paraelectric potassium niobates. These films have shown superparaelectric behavior: 5% tunability at an electric field of 100 kV/cm, losses as low as 0.3%, and excellent stability to temperature and frequency changes.

2.2.2.3. Radio Frequency (RF) Magnetron Sputtering

Magnetron sputtering is a powerful and flexible PVD coating technique which can be used to coat virtually any workpiece with a wide range of materials such as any solid metal or alloy and a variety of compounds. Prior to the magnetron sputtering coating procedure a vacuum of less than one ten millionth of an atmosphere must be achieved. From this point a closely controlled flow of an inert gas, such as argon, is introduced. This raises the pressure to the minimum needed to operate the magnetrons, although it is

still only a few ten thousandth of atmospheric pressure. A magnetron consists of a plate of the material of which all or part of the coating is to consist (referred to as the target) with magnets arranged behind it with alternating polarity as shown in Figure 2.18.
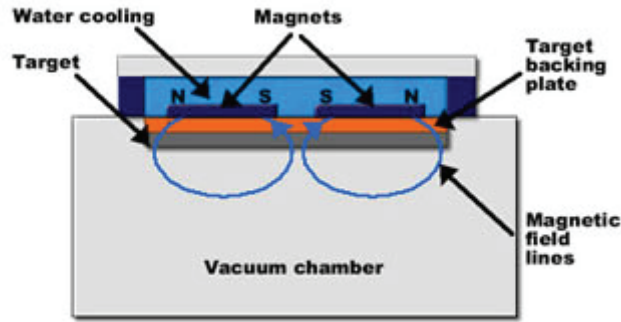
Figure 2.18 Schematic of a magnetron

When power is supplied to the magnetron a negative voltage of typically -300 V or more is applied to the target. This attracts argon ions to the target surface at speed. When they collide with the surface two important processes take place: Atoms are knocked out of the target surface with mean kinetic energies of 4 to 6 eV- this is sputtering. These sputtered atoms are neutrally charged and so are unaffected by the magnetic trap. These sputtered atoms collide with the substrates to be coated and form an extremely adherent coating. Generally the formation of the coating consists of a four stage process, nucleation, island growth, coelescence and finally continuous growth. The second important process that occurs when an ion collides with the target surface is that electrons are emitted. The light and negatively charged electrons when they leave the surface are affected by the combination of electrostatic and magnetic forces and execute cycloidal motion around the magnetic field lines. When an electron of sufficient energy collides

with a neutral atom it can knock another electron out of the atom resulting in the creation of a positive ion, ionization. This ion is attracted towards the target surface and the whole sputtering process is repeated. As the electrons are trapped by the magnetic field their path lengths and the degree of ionisation are increased. This increased ion density close to the target produces a high deposition rate (> 500 nm/min) and the electron trapping provides less free electrons to bombard the substrate resulting in the ability to coat temperature sensitive substrates.

$Na_{0.5}K_{0.5}NbO_3$ thin films have been deposited onto textured polycrystalline $Pt_{80}Ir_{20}$ substrates using radio frequency magnetron sputtering [62]. Films were grown in off- and on-axis positions relative to the target at growth temperatures of 500-700 °C and sputtering pressures of 1-7 Pa. The deposited films were found to be textured, displaying a mixture of two orientations (001) and (101). Films grown on-axis showed a prefered (001) orientation, while the off-axis films had a (101) orientation. Scanning electron microscopy showed that the morphology of the films was dependent on the substrate position and sputtering pressure. The low-frequency (10 kHz) dielectric constants of the films were found to be in the range of approximately 490-590. Hydrostatic piezoelectric measurements showed that the films were piezoelectric in the as-deposited form with a constant up to 14.5 pC/N.

Thin films of $(Na,K)NbO_x$ (NKN) were grown by reactive RF magnetron sputtering on polycrystalline $Pt_{80}Ir_{20}$ substrates, at relatively low growth temperatures between 300 °C and 450 °C [63]. The results show that the electrical performance and the microstructure of the films are a strong function of the substrate temperature. X-ray diffraction of films

grown up to 400 °C revealed the formation of only one crystalline NKN-phase with a preferred (002)-orientation. However, a mixed orientation together with a secondary, paraelectric potassium niobate phase, were observed for NKN films deposited at 450 °C. The differences in the microstructure explains the variations in the dielectric constants and losses: The single phase NKN films displayed a dielectric constant and a dielectric loss of 506 and 0.011, respectively, while the films with mixed phases exhibited values of 475 and 0.022, respectively.

$(K_x, Na_{1-x})NbO_3$ (KNN) thin films were deposited on $(001)SrRuO_3/(001)Pt/(001)MgO$ substrates by RF-magnetron sputtering, and their piezoelectric properties were investigated [64]. The x-ray diffraction measurements indicated that the KNN thin films were epitaxially grown with the c-axis orientation in the perovskite tetragonal system. The KNN thin films showed typical ferroelectric behavior; the relative dielectric constant ε_r was 270-320. The piezoelectric properties were measured from the tip displacement of the KNN/MgO unimorph cantilevers; the transverse piezoelectric coefficient e_{31} ($= d_{31}/s^E_{11}$) of KNN (x = 0) thin films was calculated to be -0.9 C/m². On the other hand, doping of potassium caused an increase in the piezoelectric properties, and the KNN (x = 0.16) films showed a relatively large transverse piezoelectricity of $e_{31} = -2.4$ C/m².

CHAPTER III

EXPERIMENTAL SETUP AND TECHNIQUES

$(K_{0.5}Na_{0.5})NbO_3$ (KNN) solution was fabricated by dissolving Na-ethoxide (Sigma-Aldrich, No. 156248), K-ethoxide (Sigma-Aldrich, No. 333379), and Nb-pentaethoxide (Sigma-Aldrich, No. 339202) as sol-gel precursors in solvents. Also, Ta-ethoxide (Sigma-Aldrich, No. 339113) was introduced as a sol-gel precursor for a doping element Ta. 2-methoxyethanol (2-MOE) (Sigma-Aldrich, No. 270482), Isopropyl alcohol, and absolute ethanol were used as solvents. Acetylacetone (Sigma-Aldrich, No. P7754) is used as a chelating agent in precursors. KNN solution was prepared under a dry nitrogen atmosphere. Various types of solvents were used to optimize the conditions to obtain lower pyrolysis temperatures for organic decomposition as well as to maintain stability against moisture during KNN solution processing and storage. In general, higher molecular weight organic precursors are decomposed at higher temperature, while the precursors become less reactive with humidity compared to lower molecular weight ones.

Detailed process step is as follows. Nb-pentaethoxide was firstly added in solvent such as 2-MOE and stirred for 1 hour at 80 °C. Subsequently, K-ethoxide was dissolved into the Nb-alkoxide added solution and stirred for 1 hour at 80 °C. Finally, Na-ethoxide was added to the Nb-, K-alkoxide solution and stirred for 1 hour at 80 °C. Initially, The concentration of mixed solution was adjusted to yield 0.3 to 0.5 M for finding optimal

coating conditions. Thermal analysis was performed to find optimal heat treatment conditions. To prepare the specimen for thermal analysis, precursor gels were synthesized from the solution and dried at 150 °C in air. For fabricating KNN films, the solution was spin-coated on 15×15 mm^2 SiO$_2$/Si(100) and Pt(111)/SiO$_2$/Si(100) substrates in air at 3,000 rpm for 30 seconds. The deposited films were subsequently dried for 8 minutes at 150 °C on a hot plate. Promptly after drying, the gel films were pyrolyzed for 10 minutes at 350 °C for the removal of organic residues. Finally, the films were annealed for 2 minutes in air at either 450, 550, 650, or 750 °C for phase transformation from pyrolyzed amorphous to crystallized perovskite phase. The coating process was repeated 15 times to increase the film thickness of about 300nm. In addition, to study the influence of pyrolized film thickness on orientation control, a buildup of pyrolyzed layers before annealing was obtained by repeating the above mentioned processes 15 times (without annealing) for KNN on Pt(111)/SiO$_2$/Si(100) substrate and 10 times for KNN on SiO$_2$/Si(100) substrate. Following the buildup of pyrolized layers, the KNN thin films were annealed for 1 hour in air at either 750, 850 or 950 °C with a ramp of 5 °C/min.

The prepared precursor gel was thermally analyzed using differential scanning calorimetry – thermogravimetry (DSC-TG, TA). Crystalline phases of the KNN thin films were confirmed by X-ray diffraction (XRD, Rigaku) and Raman Spectroscopy (JY). Their microstructures were also observed by using a field-emission scanning electron microscopy (FE-SEM, JEOL). Furthermore, P-E hysteresis loops of KNN films were measured by using a ferroelectric tester (aixACCT Systems, TF 2000).

CHAPTER IV

RESULTS AND DISCUSSION

4.1. Optimized Conditions of KNN Precursor Solution

Five different solvent and chelating agent combinations were used to obtain optimized solution for the fabrication of KNN thin films as follows:

1) 2-Methoxyethanol (2-MOE)

2) 2-Methoxyethanol (2-MOE) + Acetylacetone (AcAc)

3) Isopropanol

4) Isopropanol + Acetylacetone (AcAc)

5) Absolute ethanol + Acetylacetone (AcAc)

According to Figure 4.1, the KNN solution fabricated by 2-MOE and AcAc is much more clear than that fabricated by 2-MOE only without using a chelating agent. The opaque color of solution can be due to aggressive reaction between alkoxide and the water-molecule diffused from the surrounding air. Typically, the acetate, or in general, the carboxylic acid groups, coordinate the metal species in a bidentate fashion, and frequently act as bridging ligands, linking metal centers together to form oligomers.

Chelation of the alkoxides by these carboxylate groups results in the formation of precursors that possess reduced sensitivity toward hydrolysis, resulting in solutions that are more easily handled in air. Also, compared to the typical 2-methoxyethanol processes, hybrid processes offer the advantages of relatively simple solution synthesis, i.e. distillation and refluxing strategies are normally not required [54]. Figure 4.2 shows the molecular structures generated by the potential chemical reactions from the addition of chelating agent AcAc.
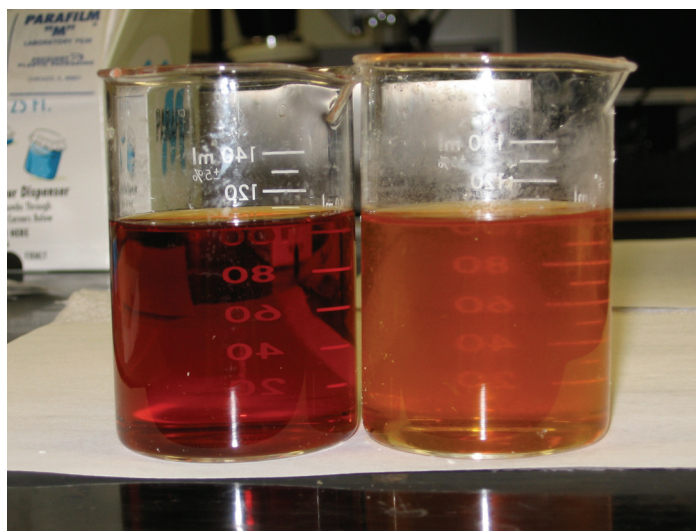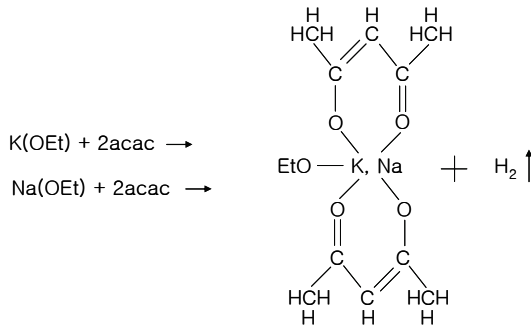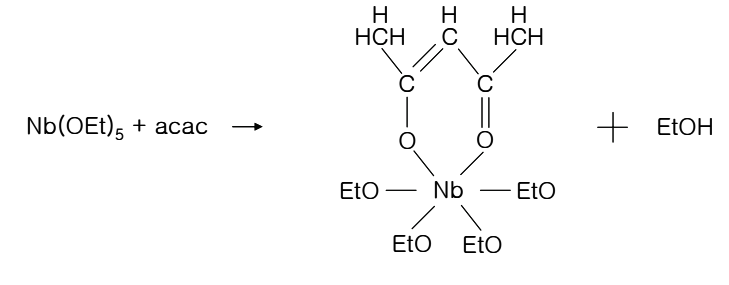

Figure 4.1 Picture for the comparison of the homogeneity of KNN solutions due to the chelating agent AcAc. Left solution is fabricated by mixing 2-MOE and AcAc and right one is solution with using only 2-MOE.

2 : 1 mixture of acac : CH_3CH_2OK or CH_3CH_2ONa

1 : 1 mixture of acac : $Nb(OCH_2CH_3)_5$

K(OEt) + 2acac →

Na(OEt) + 2acac →

$+ H_2 \uparrow$ Nb(OEt)$_5$ + acac →

$+$ EtOH

(a)   (b)

Figure 4.2 The molecular structures created by possible chemical reactions due to the addition of chelating agent AcAc in the case of (a) K or Na-ethoxide and (b) Nb-pentaethoxide.

The commercial Na-ethoxide (Sigma-Aldrich, 230553) and K-ethoxide (Sigma-Aldrich, 515051) were also diluted in absolute ethanol based on the assumption that absolute ethanol might be better for preparing well-dispersed KNN solution in comparison with 2-MOE. Also, from the published report, $(K_{0.5}Na_{0.5})NbO_3$ solution was successfully fabricated by the absolute ethanol and perovskite phases of KNN were created [65]. However, in this experiment the distinguishable difference between the KNN solutions fabricated by 2-MOE and absolute ethanol was not found. Isopropanol was also investigated since isopropanol is expected to be intermediate between ethanol and 2-MOE when considering molecular weight. However, some agglomerations were observed during solution fabrication. It appears that isopropanol might not be an appropriate solvent with K, Na, and Nb-ethoxide precursors for the KNN precursor

solution. It can be due to incomplete reaction between metal ethoxide precursors and ethyl branch in the solvent, which cause excessive hydrolysis reaction for precipitation.

To investigate the effects of the homogeneity of solution on the deposition of KNN thin film, KNN thin films were prepared by coating different KNN solutions fabricated by 2-MOE + AcAc and Isopropanol on silicon-based substrates and performing heat treatment. The surface conditions of KNN thin films are compared in Figure 4.3.
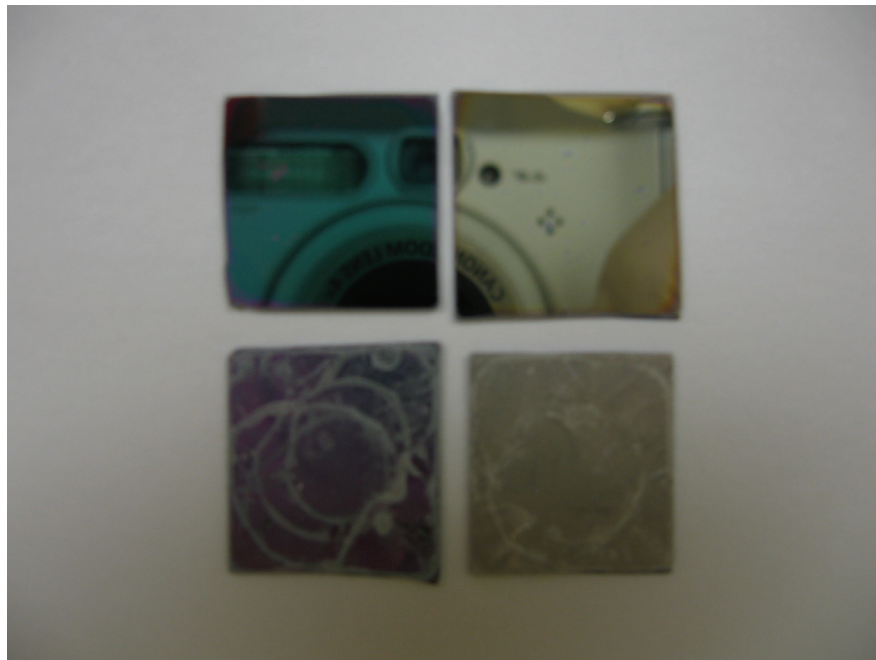
Figure 4.3 The comparison of the surface conditions of KNN thin films fabricated by two different solutions. From the upper left corner the experimental conditions are sequentially 2-MOE + AcAc on the Si/SiO_2 (500 nm) substrate and 2-MOE + AcAc on the $Si/SiO_2/Ti$(10 nm)/Pt(120 nm) substrate. From the lower left corner the experimental conditions are subsequently Isopropanol on the Si/SiO_2 (500 nm) substrate and Isopropanol on the $Si/SiO_2/Ti$(10 nm)/Pt(120 nm) substrate.

Based on Figure 4.3, 2-MOE + AcAc shows a good wetting property on the substrate and the surface of KNN thin films is smooth like a mirror, whereas Isopropanol shows a poor wetting property and the surface is rough. The results manifest that the condition of KNN thin films strongly depends on the types of precursor solution.

4.2 Thermal Studies of KNN Precursor Gels

The most stable solution system consisting of 2MOE-AcAc was analyzed to investigate the types of bonding and to determine heat treatment conditions for thin film formation. Figure 4.4 illustrates the results of differential scanning calorimetry (DSC) and thermogravimetric analysis (TGA) curves of KNN precursor gels dried at 150 °C. The weight of the dried gel rapidly decreased until around 90 °C where a large endothermic peak emerged. This peak was associated with the evaporation of water contained in the gel. The peak at 335 °C may be caused by decomposition of metal alkoxides and hydrocarbons. The peak at 500 °C may arise from the combustion of residual carbon. The strongest peak at 550 °C is due to the crystallization of the KNN thin film without massive volatilization of alkaline oxides which can be confirmed because there is no corresponding weight loss in the TGA curve. The TG-DTA curve obtained by K. Tanaka et al. [18] showed rapid decrease in weight at about 470°C to 550 °C and total decrease of weight for both precursor gels were estimated to be about 15.5%. On the other hand, the gradual loss in weight about 28.1 % until 500 °C was presented shown in Figure 4.4. Also, the TG-DTA results from K. Tanaka et al. show that slight decrease of weight after the carbon combustion is likely due to volatilization of Na and/or K-based compounds, since endothermic and exothermic peaks did not emerge in the temperature range 550 to

800 °C. Conversely, the TGA results shown in Figure 4.4 do not show distinct decrease in weight so that volatility of K and Na oxides could not be confirmed. As I will mention in the section 4.5, P-E hysteresis loops of KNN thin films with excess K and Na ions show reduced leakage current. Thus, the DSC-TG measurement equipment may have limitation to measure small amount of volatile K and Na ions while electrical properties such as P-E hysteresis loop was strongly influenced by the existence of such a defect.
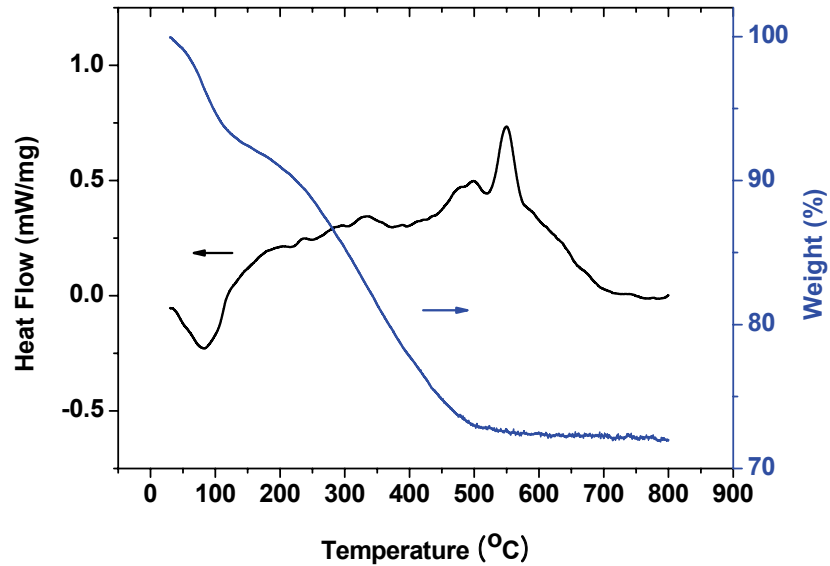

Figure 4.4 DSC-TG curves of the $(K_{0.5}Na_{0.5})NbO_3$ dried gels.

4.3. Phase Analysis of KNN Thin Film

4.3.1. Perovskite Phase Identity

   The XRD patterns of KNN thin films annealed at temperatures ranging from 450 °C to 750 °C on (a) Pt(111)/SiO$_2$/Si(100) and (b) SiO$_2$/Si(100) substrates are shown in Figure 4.5. Crystalline phases began to appear from 550 °C and upward as seen in the (100) peaks at 22.5 ° and the (200) peaks at 46.1 °, very close to the temperature estimated from DSC-TG. These results demonstrate KNN crystalline thin films may be grown on both substrates at lower annealing temperatures by sol-gel processing. The results are consistent with previous report [18]. Furthermore, at elevated temperature, the intensities of the (100) and (200) peaks increased meaning that higher annealing temperatures exponentially enhanced the nucleation and growth rate. As a structural viewpoint, KNN ceramics have an orthorhombic structure at room temperature. Lattice parameters for KNN (a = 0.3994 nm, b = 0.4016 nm and c = 0.3935 nm) were reported by Singh *et al*. [6]. However, by assuming KNN thin films have pseudo-cubic structure, the calculated lattice parameter of KNN annealed at 750 °C was in the range of 0.3925 to 0.3958 nm from the peaks appeared at 22.5 °, 32 ° and 46.1 °. This result is consistent with the earlier research [18]. Figure 4.5 (c) shows that there is the second phase K$_4$Nb$_6$O$_{17}$ about 27.5 ° as K. Tanaka et al. reported [17]. The authors considered that the sodium-free secondary phase formed because the volatilization rate of Na$_2$O was higher than that of K$_2$O. They used the basic kinetic theory to explain that the speed of volatilization of Na$_2$O would be higher than that of K$_2$O, since the speed of the molecules are inversely proportional to the root-square of the molecular weight and the molecular weight of Na$_2$O is lower than that of K$_2$O. This could be one possibility from XRD results obtained by the

KNN thin films fabricated by KNN solutions with the excessive K and Na ions as shown in Figure 4.5(d).
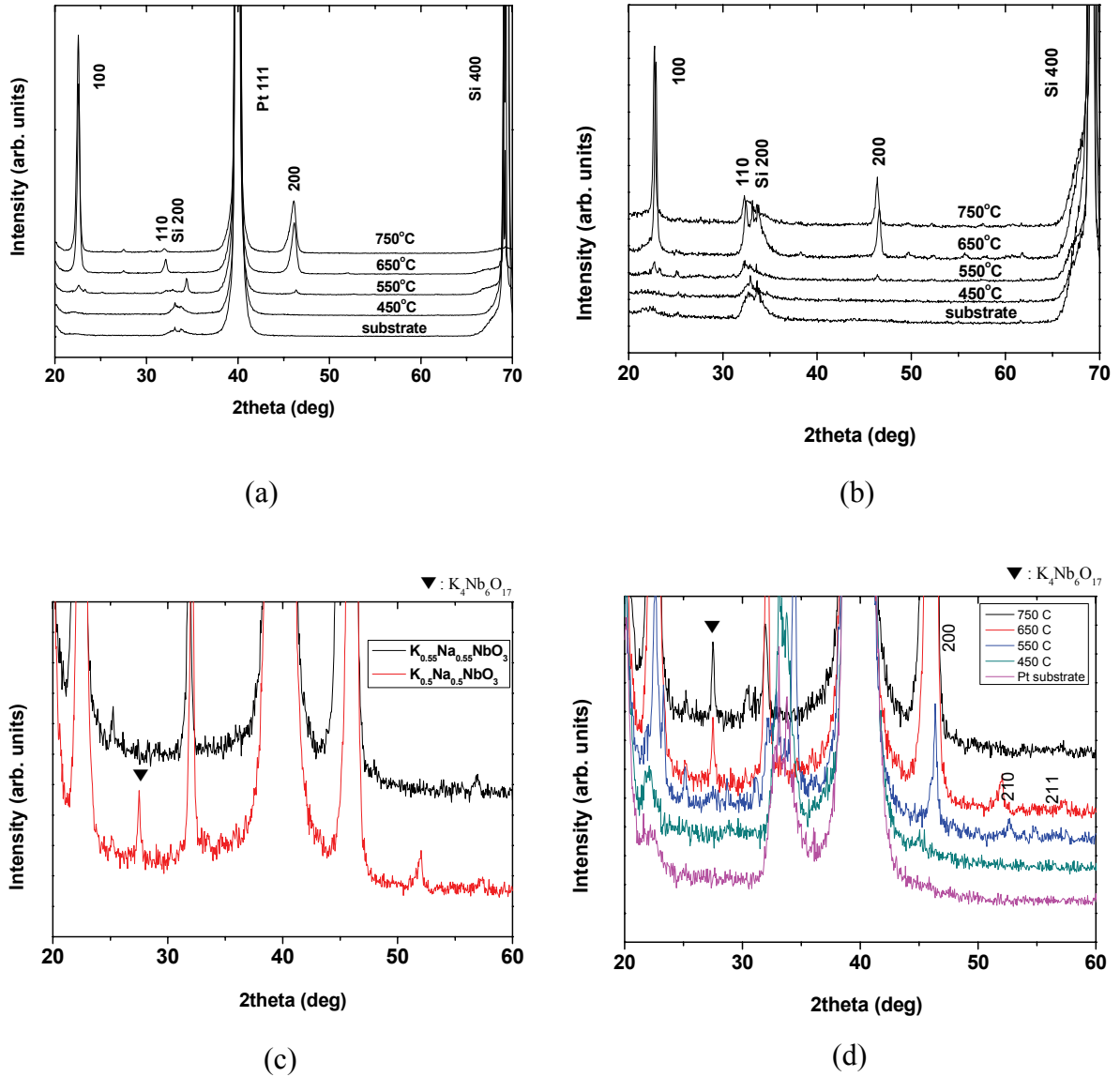

(a)

(b)

(c)

(d)

Figure 4.5 XRD patterns of the $(K_{0.5}Na_{0.5})NbO_3$ thin films fabricated at 450 °C to 750 °C on (a) Pt(111)/SiO$_2$/Si(100) and (b) SiO$_2$/Si(100) substrates and (c) XRD peaks to show the occurance of the second phase and (d) its disappearance due to the excessive A site ions.

As mentioned in the section 4.1, the KNN solution was also fabricated by using absolute ethanol as a solvent. KNN thin films were synthesized by KNN solution prepared by absolute ethanol in the same condition as that dissolved by 2-MOE. Figure 4.6 shows the XRD peaks corresponding to perovskite phases of the KNN film. Also, the peak at around 29° is observed, shows that a secondary phase may appear.
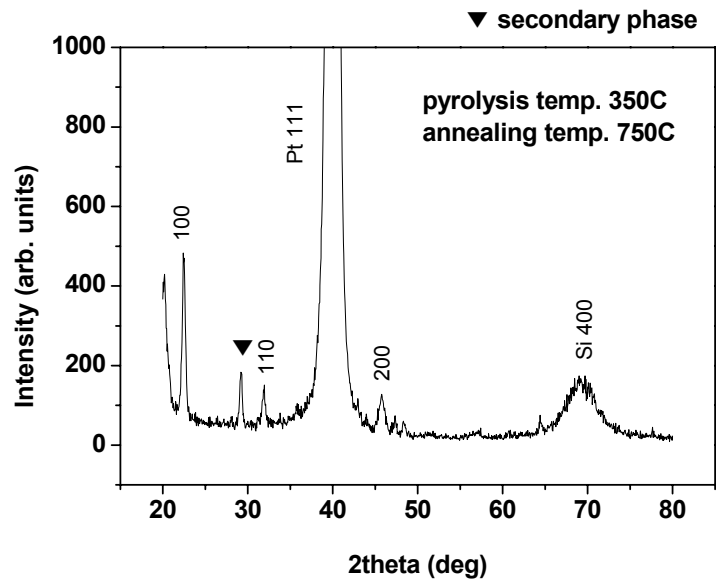

Figure 4.6 XRD patterns of KNN thin films fabricated by solvent absolute ethanol.

If there is a powder formation during KNN solution preparation, KNN thin films result in severe leakage currents at P-E hysteresis loops as I will mention in the section 4.4. It was assumed that the problem would stem from the inhomogeneous solution conditions of initial KNN solution. In particular, while the powder formed precursors were dissolved in the 2-MOE under the glove box, serious reaction of precursors with moisture could be found. As a result, the precursors were deteriorated and badly affected

the KNN solution such as inhomogeneity. Thus, diluted K and Na – ethoxide precursors in the ethanol 21 wt% were introduced during the fabrication of KNN solutions. As might be expected, their severe reaction with moisture in the glove box would be effectively reduced. As can be seen in Figure 4.7, for all the compositions of KNN, perovskite phases appeared. In addition, like previous data, the KNN thin films are grown with the preferred orientation along (100) orientation. However, it appears that there are more complicated reactions depending on the types of precursors. Although the powder or particle formation was reduced, the electric properties were not improved as will be discussed in Figure 4.17, which will require further detailed investigation.
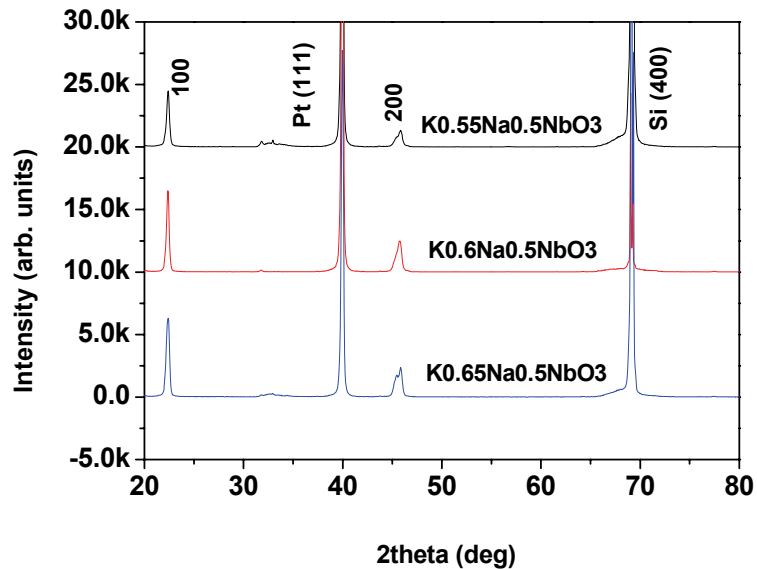

Figure 4.7 XRD patterns for the KNN thin films fabricated by diluted K and Na – ethoxide precursors and annealed at 750°C with various compositions.

In addition to X-ray analysis, Micro-Raman spectroscopy was performed to further investigate the degree of crystallization of the $(K_{0.5}Na_{0.5})NbO_3$ thin films. Figures 4.8(a) and 4.8(b) show Raman spectra of $(K_{0.5}Na_{0.5})NbO_3$ thin films deposited on (a) Pt(111)/SiO$_2$/Si(100) and (b) SiO$_2$/Si(100) substrates, followed by annealing at 450 °C, 550 °C, 650 °C, and 750 °C under oxygen atmosphere. Note that the intense peak located at 520 cm^{-1} (Figure 4.8(b)) is produced by Raman scattering from the Si substrate. Recently, Kakimoto *et al*. [66] has reported Raman spectra of the $(K_{0.5}Na_{0.5})NbO_3$ powder. As shown in both Figures 4.8(a) and 4.8(b), our Raman spectra collected from the samples annealed at 650 °C and 750 °C exhibit similar features to those of the KNN powder. The peaks at around 245 cm^{-1} and 610 cm^{-1} are attributed to ν_5 and ν_1 vibrational modes of NbO_6 octahedra, respectively [66]. As can be clearly seen from the figures, the Raman spectra collected from the samples annealed at 650 °C and 750 °C did not exhibit any substantial difference, which is consistent with the result obtained from the X-ray diffraction study. The Raman results imply that a crystallized phase was formed when annealed at those temperatures.
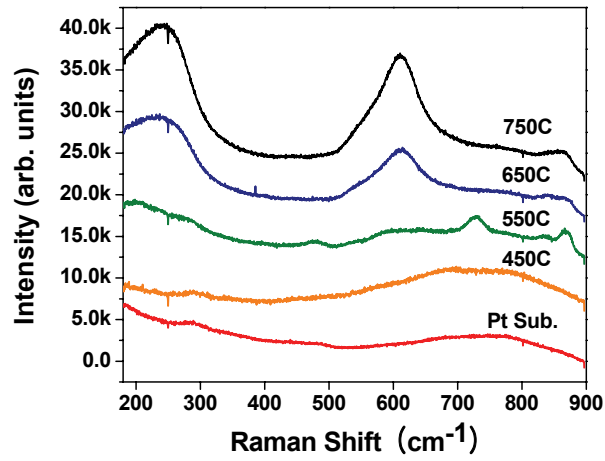
(a)
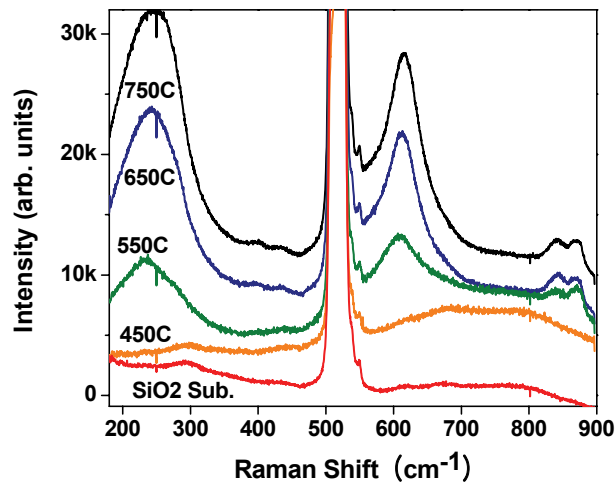
(b)

Figure 4.8 Raman spectra of $(K_{0.5}Na_{0.5})NbO_3$ thin films deposited on (a) Pt(111)/SiO_2/Si(100) and (b) SiO_2/Si(100) substrates, followed by annealing at 450 – 750 °C (The Raman spectra collected from the substrates are also shown for comparison.).

4.3.2. Orientation Control

In Figure 4.5, KNN thin films grown on both $Pt(111)/SiO_2/Si(100)$ and $SiO_2/Si(100)$ substrates resulted in a textured orientation along the c-axis, corresponding to [001] directions. This result can be explained by considering surface energy of crystallographic planes and nucleation and growth mechanism for phase transformation.

From the calculation by Cho and his coworkers on the surface energy of the principal planes such as (100), (110), and (111) of KNN [8], , the surface energy of (100) is much lower than that of (110).

According to nucleation and growth theory as expressed by Eqs. (1) and (2), the energy barrier of nucleation is proportional to the cube of the surface energy of the plane. Thus, nucleation will preferentially occur along the (100) plane for both homogeneous and heterogeneous conditions.

$$\Delta G^*_{Homo} = \frac{16\pi\gamma^3}{3(\Delta G_V + \Delta G_e)^2} \qquad \text{...... (1)}$$

and

$$\Delta G^*_{Hetero} = \Delta G^*_{Homo} \times f(\Theta) = \frac{16\pi\gamma^3}{3(\Delta G_V + \Delta G_e)^2} \times f(\Theta) \qquad \text{...... (2)}$$

where γ, ΔG_V, ΔG_e, and $f(\Theta)$ are the interfacial energy of the newly formed interface, the difference in volume free energy, the elastic strain energy, and geometry factor which

is determined by the surface energies of the film and the substrate. The interface between the pyrolyzed film and the substrate offers opportunities for heterogeneous nucleation and growth to obtain a textured orientation. The 20 − 30 nm thick as-deposited layers could allow the interface-nucleated grains to efficiently reach the surface of the next layer within a short time. These thin layers appear to serve as seeding layers to decrease the activation energy for nucleation and growth of the KNN thin films during layer-by-layer annealing. On the other hand, in the case of KNN thin films annealed only once at 950 °C, the XRD peaks indicate a random orientation considering the relatively stronger intensity of the (110) peak as shown in Figure 4.9. As mentioned previously, the KNN thin film was pyrolyzed after each layer was deposited before the final annealing step. For thicker pyrolized layers, the time required for the nucleation and growth of the interface-nucleated grains to reach the opposing surface would be greater than for thinner layers during annealing [67]. Furthermore, at higher temperatures, since the energy barriers will be sufficiently overcome, homogeneous nucleation and growth may easily occur inside of the thin films. As a result, a random orientation similar to bulk KNN ceramics was observed [1]. Microstructure variations of heterogeneous and homogeneous nucleation and growth with film growth are depicted in Figure 4.10. Cross-sectional SEM micrographs of KNN thin films generated by (c) heterogeneous (a columnar microstructure) and (d) homogeneous (a non-columnar microstructure) nucleation and growth demonstrate the proposed microstructural evolution.
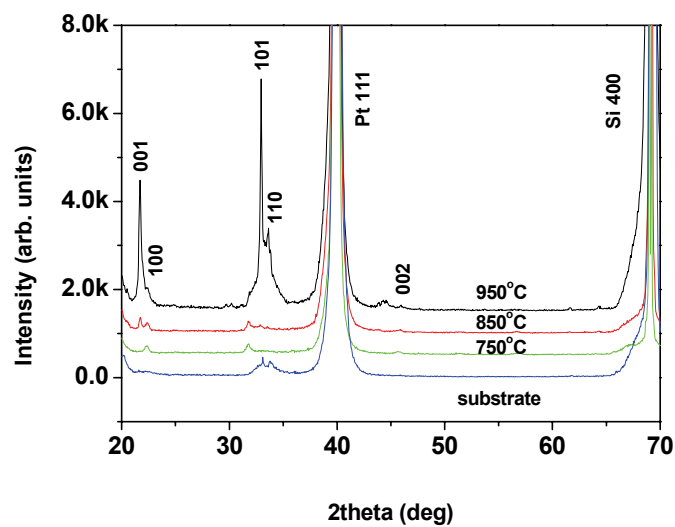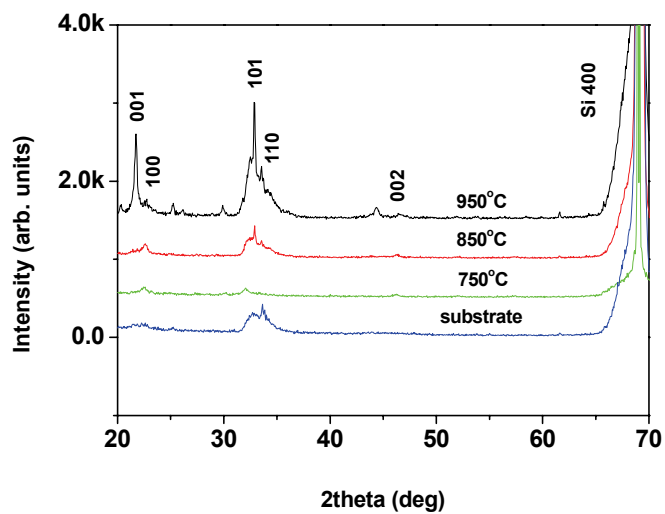
Figure 4.9 XRD patterns for 320 nm thick KNN thin films grown on (a) Pt(111)/SiO$_2$/Si(100) and (b) SiO$_2$/Si(100) substrates single annealed at 750 °C to 950 °C. The heating rate is 5 °C/min and the annealing time is 1 hour.
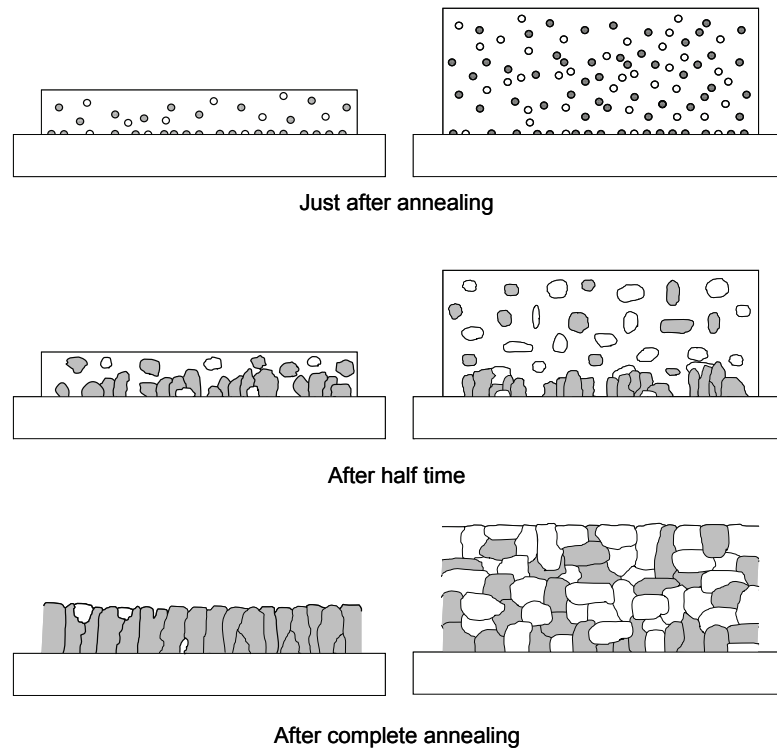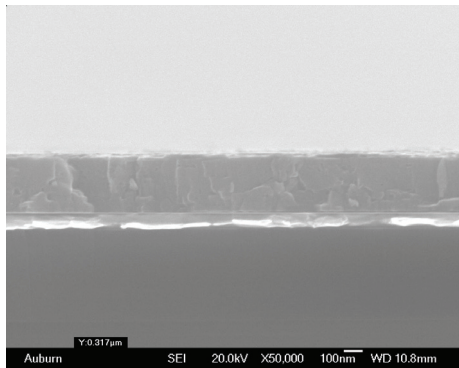
Figure 4.10 The schematic diagram to show (a) heterogeneous and (b) homogeneous nucleation and growth of KNN thin films as a function of annealing time. The corresponding SEM micrographs of KNN thin film microstructure generated mainly by (c) heterogeneous or (d) homogeneous nucleation and growth.

To compare these different results quantitatively, the degree of c-axis orientation (D_c) can be calculated by the following equation.

$$D_c = \frac{I_{(100)}}{I_{(100)} + I_{(110)}}$$

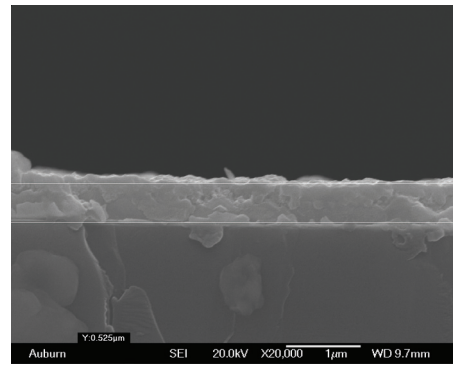where $I_{(100)}$ and $I_{(110)}$ are the intensities of the XRD peaks for the (100) and (110) planes of the KNN, respectively. Specifically, D_c of KNN thin films coated on Pt(111)/SiO$_2$/Si(100) substrate at an annealing temperature 750 °C for 15 times and one time were 98 % and 36 %, respectively. To date, KNN thin films deposited by sol-gel processing have shown both textured [17-18] and random [19-20, 68] orientations as summarized in Table 4.1. From these data and reported results, the thickness of the pyrolized layer increases before annealing mainly causes random orientation of KNN films.

Table 4.1 Summary of solution derived KNN films previously reported.

A site ion ratio (Na/K)	Concentration of solution (mol/L)	Thickness per layer (nm)	Pyrolysis	Sintering	Heat treatment	Total thickness (nm)	Substrate	Orientation	Reference
50/50, 52/52, 55/55, 58/52, 60/50	0.35	25	350 °C for 5 min	600 °C for 1 min (RTA 300 °C/min)	layer–by–layer	~250	Pt/Ti/SiO$_2$/Si	textured (100) orientation	17
50/50	0.3	25	350 °C for 3 min	450 – 700 °C for 1 min (RTA 50 °C/sec)	layer–by–layer	~250	SiO$_2$/Si(100)	textured (100) orientation	18
52/52, 55/55	0.5	Not mentioned	300 °C at a rate of 10 °C/min then heating at 300 °C for 30 min	500, 600 or 650 °C for 10 or 60 min	layer–by–layer	~600	Pt/TiO$_x$/SiO$_2$/Si	random orientation	19
50/50, 51/51, 52/52, 55/55	0.5	Not mentioned	300 °C (10 °C/min) for 30 min	650 °C (10 °C/min) for 10 min	layer–by–layer	~600	Pt/TiO$_x$/SiO$_2$/Si	random orientation	20
50/50, 50/80	0.4	100	From 200 to 500 °C for 3 min	From 700 to 900 °C (from 70 to 90 °C/sec) for 1 min	pyrolysis of all layers and final crystallization	~500	amorphous ZrO$_2$ buffer layer / Si(100)	random orientation	21

4.3.3 Microstructures of KNN Thin Film

Figure 4.11 presents microstructures of KNN thin films annealed at 450 °C to 750 °C. It can be assumed that microstructures of KNN thin films were most likely determined by not only annealing temperatures but also the types of substrates. The average grain size (e.g. diameter) was calculated from the number of grains in 1.21×1.14 μm^2 area from SEM micrographs, assuming each grain was a sphere. As seen in Figure 4.11, microstructure evolution was strongly dependent on annealing temperatures instead of the type of substrates. The average grain size increased with annealing temperature. For both Pt(111)/SiO$_2$/Si(100) and SiO$_2$/Si(100) substrates, the grain size increased from around 160 nm to around 200 nm as the annealing temperature increased from 650 °C to 750 °C.

4.4 Ferroelectric Hysteresis of KNN Thin Film

P-E hysteresis loops of the KNN thin film on Pt(111)/SiO$_2$/Si(100) substrate were obtained at 1 kHz and room temperature as shown in Figure 4.12. Although hysteresis loop of KNN film were measured at the field over 250 kV/cm,the loops were not completely saturated due to some leakage current in the film. The KNN thin film showed the 2P$_r$ and 2E$_c$ values of 19 $\mu C/cm^2$ and 200 kV/cm, respectively. The incomplete saturation in the loop can be attributed to the oxygen vacancies formed by the loss of volatile A site ions such as Na and K.

(a)　　　　　　　　　　(b)　　　　　　　　　　(c)

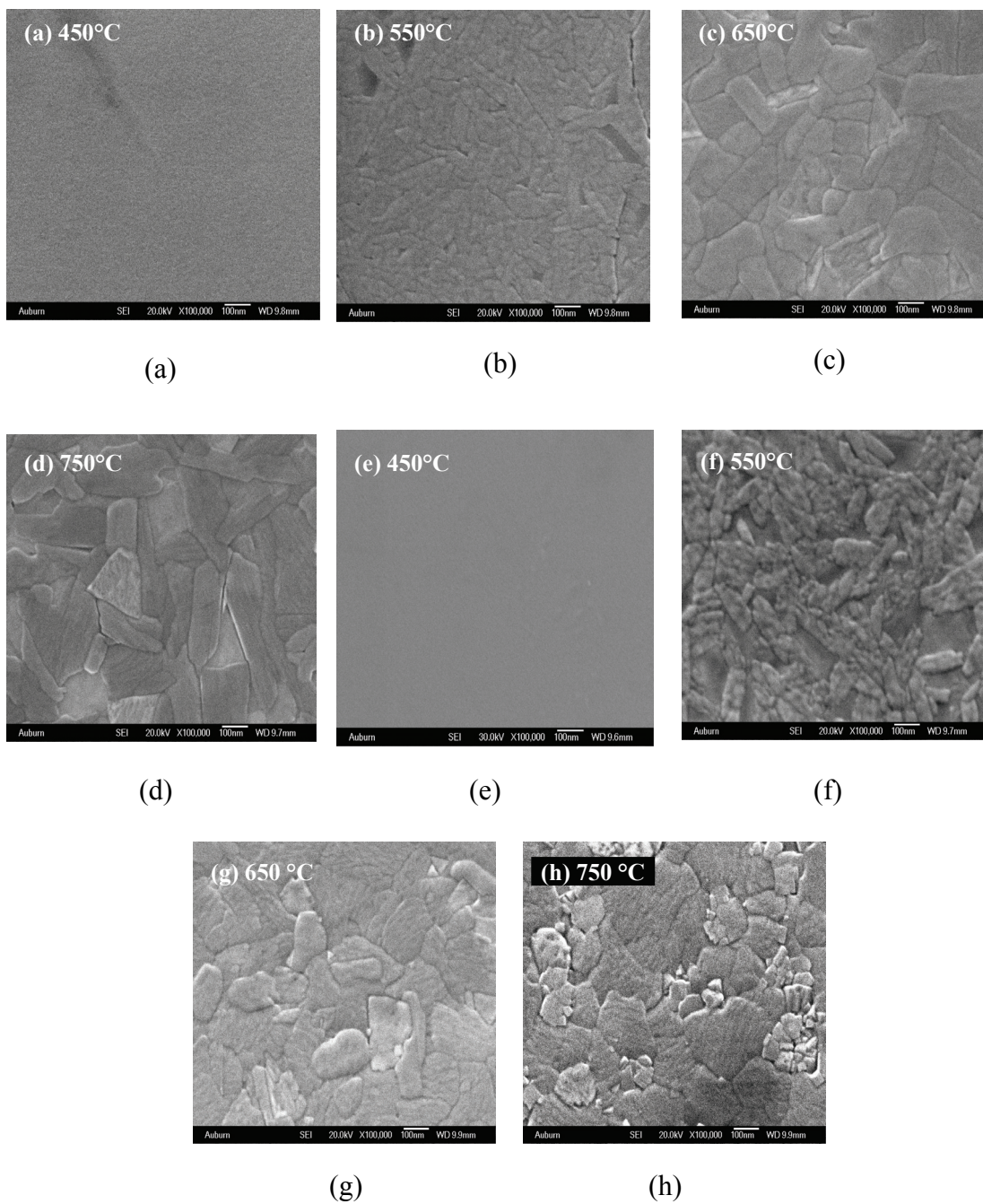(d)　　　　　　　　　　(e)　　　　　　　　　　(f)

(g)　　　　　　　　　　(h)

Figure 4.11 SEM micrographs of the $(K_{0.5}Na_{0.5})NbO_3$ thin films fabricated at 450 °C to 750 °C on (a) – (d) Pt(111)/SiO$_2$/Si(100) and (e) – (h) SiO$_2$/Si(100) substrates.
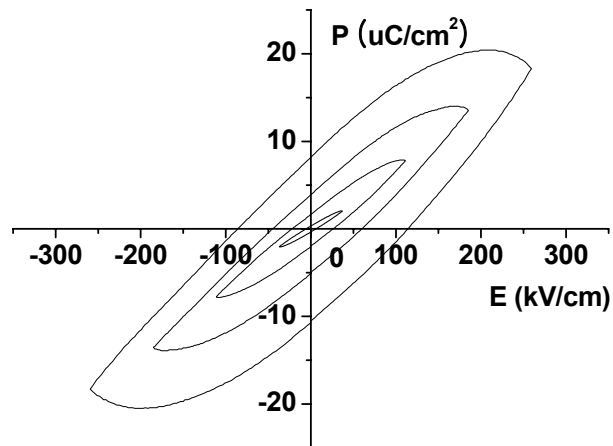
Figure 4.12 Ferroelectric P-E hysteresis loops for 320 nm thick $K_{0.5}Na_{0.5}NbO_3$ thin films fabricated at 750ºC on Pt(111)/SiO$_2$/Si(100) substrates.

4.5 Nonstoichiometry of KNN Due to the Volatility of Na$_2$O and K$_2$O

The volatile oxides Na$_2$O and K$_2$O in KNN system can affect the stoichiometry and deteriorate its electrical properties such as unsaturated polarization caused by leakage current. In order to investigate the volatility of A-site cations, the amount of excessive K and Na ions was varied, and the effects on film crystallinity were investigated by XRD. Although adding excess A site ions would deteriorate perovskite structures of KNN thin films, the 10 mol% excessive K and Na added KNN thin films still show the perovskite strucutre, as can be seen in Figure 4.13. Also, there is no significant influence of excessive A site ion on the orientation, i.e. films with excess A site ions still show strong (100) orientation.
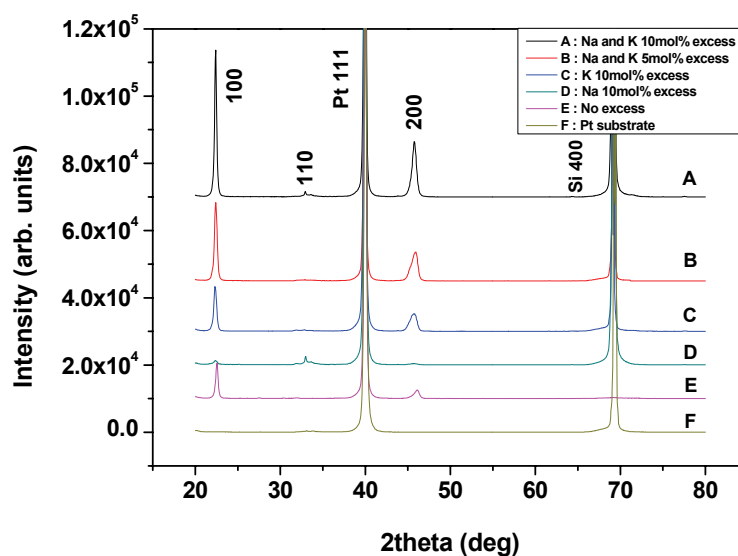
Figure 4.13. XRD patterns of the KNN thin films fabricated at 750 °C on Pt(111)/SiO$_2$/Si(100) substrates from precursor solutions with various K/Na ratios.

The degree of volatility between K$_2$O and Na$_2$O in KNN can be explained in terms of the thermodynamics. The standard Gibbs free energy of formation for two K$_2$O and Na$_2$O is as follows:

$$4Na + O_2 \rightleftarrows 2Na_2O$$

$$4K + O_2 \rightleftarrows 2K_2O$$
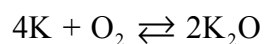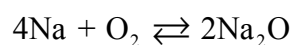
Based on Ellingham Diagram reported from the report of Department of Energy (DOE) [69], the standard Gibbs free energy of Na$_2$O is lower than that of K$_2$O at same

temperature. This means that Na ions can be more easily oxidized than K ions so that K ions may be more likely to be reduced than oxidized compared to Na_2O. Furthermore, since the standard Gibbs free energy for Nb_2O_5 is lower than that of Na_2O and K_2O, Nb_2O_5 is thermodynamically most stable so that it will be less volatile. The assumption is consistent with the results from the NIST-JANAF Thermochemical Tables [70].

The volatile K and Na ions can cause the formation of oxygen vacancies in order to maintain the charge neutrality in KNN thin films. On the other hand, the 5 to 10 mol% excessive A site ions in the KNN could compensate for the volatile ones during annealing and suppress the formation of the oxygen vacancies caused by volatile A site ions. As a result, stoichiometric KNN compositions will be maintained, and thus creating well saturated P-E hysteresis loops.

In Figure 4.14, P-E hysteresis loops for $K_{0.55}Na_{0.55}NbO_3$ thin films on $Pt(111)/SiO_2/Si$ (100) substrates were shown according to diverse conditions of annealing temperatures. The measurements were conducted at switching frequency of 1 kHz and room temperature.

From Figure 4.14, the leakage currents have been decreased with the increase of annealing temperatures. In particular, P-E hysteresis loops approach to the typical P-E curve at the annealing temperature of 750 ℃. It is considered that the improved crystallization of KNN phase occurs with the increase of annealing temperature.

However, based on Figure 4.14(d), the complete saturation could not be obtained probably due to leakage current that may be attributed to the nonstoichiometry caused by volatile A site ions. Therefore, various compositions of excessive A site ions were studied in order to obtain the condition for best ferroelectric properties.
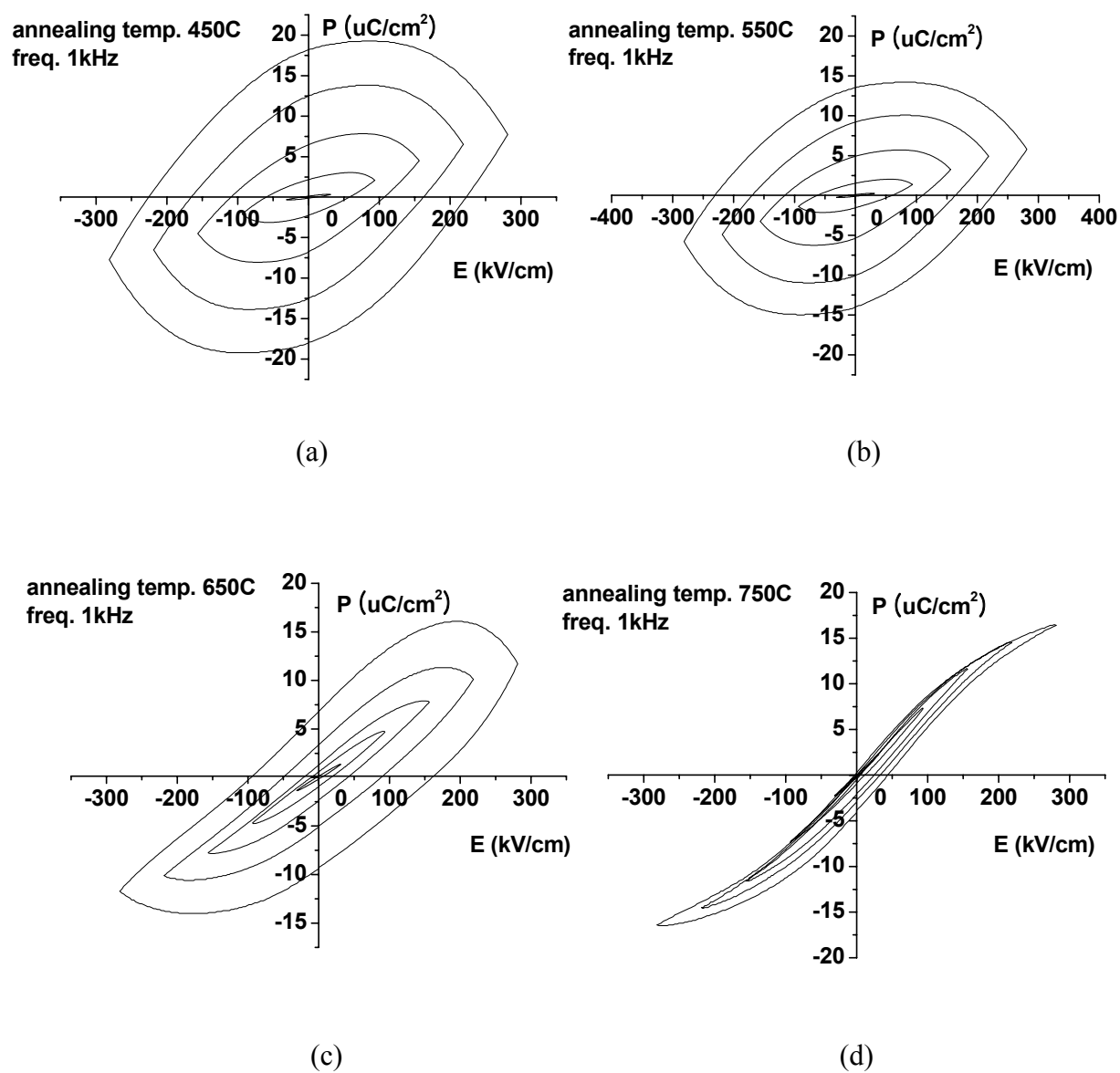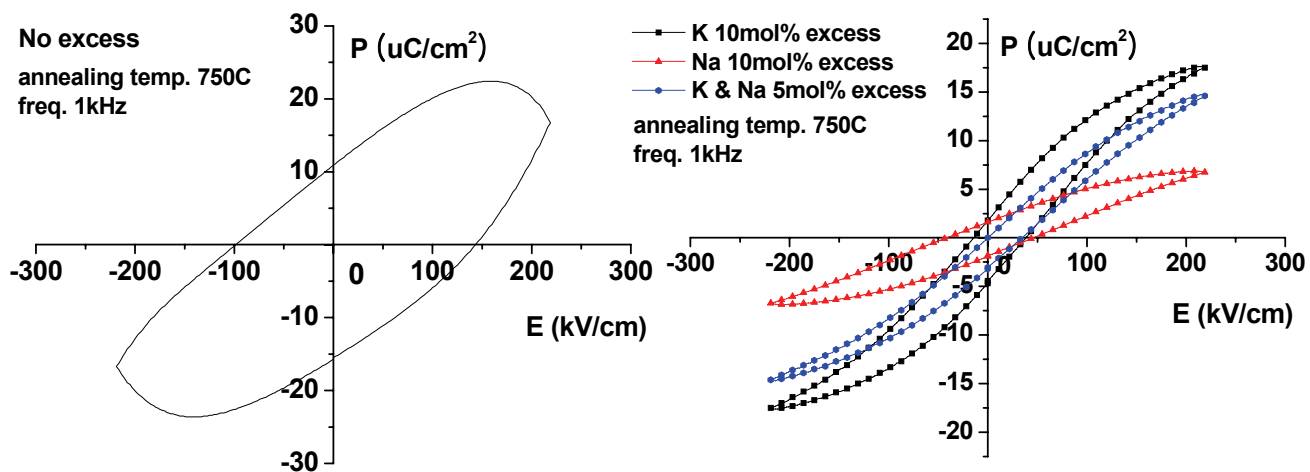
Figure 4.14. P-E hysteresis loops of $K_{0.55}Na_{0.55}NbO_3$ thin films fabricated at 450 to 750ºC on Pt/SiO$_2$/Si substrates.

In Figure 4.15, P-E hysteresis loops of KNN thin films on Pt(111)/SiO$_2$/Si(100) substrates were presented according to the diverse excessive A site ions. The measurements were carried out at switching frequency 1 kHz and room temperature.
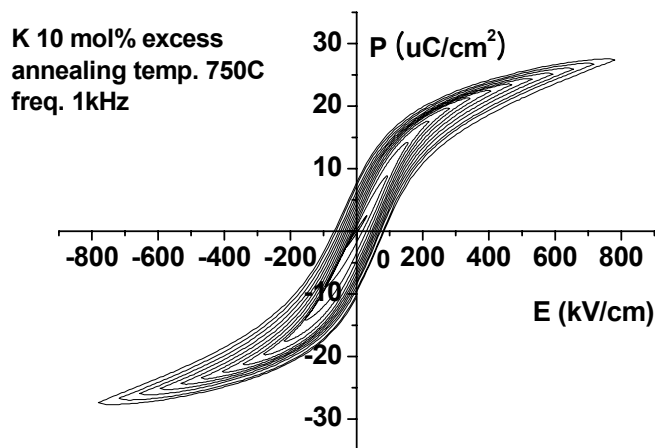
For no excess K$_{0.5}$Na$_{0.5}$NbO$_3$, the P-E hysteresis loops were not completely saturated due to some leakage current in the films. However, 10 mol% excessive K ions K$_{0.6}$Na$_{0.5}$NbO$_3$ could tolerate higher applied electric fields over 800 kV/cm showing almost typical P-E hysteresis curves. The 2Pr, and 2Ec values at the field of 800 kV/cm are approximately 17.5 μC/cm^2 and 150 kV/cm, respectively. From the literature, Y Nakashima et al. reported the 2Pr and 2Ec values are 14 μC/cm^2 and 140 kV/cm, respectively, which are relatively smaller than ours [20]. Also, the result from K. Tanaka et al. showed paraelectric-like linear P-E curve [17]. Furthermore, for 10 mol% excessive Na ions, the saturated P-E hysteresis loops were not attained due to leakage current so that they could not be comparable to 10 mol% excessive K ions. Overall, the results prove that K ions can be more volatile components during annealing process compared to Na ions, and play more significant role in KNN compositions showing the better saturated P-E hysteresis loop. The results are in contrast with ones by Tanaka et al. [17] claiming that Na ion in KNN is more volatile than K ion. Detailed investigation on the degree of volatility of Na and K ions, and their effects on properties should be performed for further study.

All P-E hysteresis loops were asymmetric, which may be due to asymmetric distribution of defects in the film. In particular, for 5 mol% excessive K and Na ions K$_{0.55}$Na$_{0.55}$NbO$_3$, the ratio of the negative Pr (-5.48 μC/cm^2) to the positive Pr (1.52 μC/cm^2) is almost 3.6, whereas for 10 mol% excessive K ions K$_{0.6}$Na$_{0.5}$NbO$_3$, the

(a)

(b)

(c)
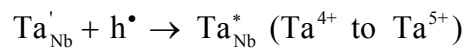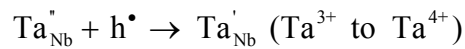
Figure 4.15 The P-E hysteresis loops of the 320nm thick KNN thin films annealed at 750°C with (a) no excess $K_{0.5}Na_{0.5}NbO_3$ (b) various compositions which are indicated at the upper left side, and (c) composition $K_{0.6}Na_{0.5}NbO_3$.

negative Pr (-9.66 $\mu C/cm^2$) to the positive Pr (7.81 $\mu C/cm^2$) is almost 1.24. Also, for

$K_{0.55}Na_{0.55}NbO_3$, the ratio of the positive Ec (60.8 kV/cm) to the negative Ec (-16.2

kV/cm) is 3.75, while for $K_{0.6}Na_{0.5}NbO_3$, the ratio of the positive Ec (85.5 kV/cm) to the

negative Ec (-70.2 kV/cm) is 1.22. Main reason for such an asymmetry might come from

the segregated movement of oxygen vacancies toward negative electrodes.

At higher temperature of 650 or 750 °C, the K and Na ions are easily volatile so that

they generate oxygen vacancies $V_O^{\bullet\bullet}$. Based on the paper of Yoichi Kizaki et al. [71], as

the second stage, the leakage current of KNN crystals is governed by electron-hole ($h^\bullet$)

conduction (p-type) as expressed by

$$V_O^{\bullet\bullet} + \tfrac{1}{2}O_2 \rightarrow O_O^* + 2h^\bullet$$
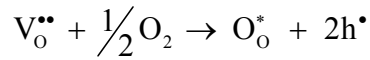
When KNN crystals absorb oxygen into the lattice, the oxygen occupies $V_O^{\bullet\bullet}$ as O_O^*

accompanied by the formation of $2h^\bullet$. Consequently, the hole is a detrimental carrier of

leakage current of KNN crystals in an oxidation state. To absorb the holes, doping

element such as Ta can be introduced in further oxidation process by the increase in

valence of Ta as expressed by

$$Ta_{Nb}^{''} + h^\bullet \rightarrow Ta_{Nb}^{'} \ (Ta^{3+} \ to \ Ta^{4+})$$

$$Ta_{Nb}^{'} + h^\bullet \rightarrow Ta_{Nb}^* \ (Ta^{4+} \ to \ Ta^{5+})$$

where the oxidation states of Ta are 3, 4 and 5.

Thus, low leakage current can be expected for Ta-KNN thin films in a wide oxidation range as a result of the increase in Ta valence absorbing holes. Ta was doped into KNN solution by 30 mol% whose amount was determined by the previous report [72].

Figure 4.16 shows the XRD results from Ta-doped KNN thin films. The strong peak around 29° to indicate pyrochlore phase is emerged in contrast to the previous result [72].
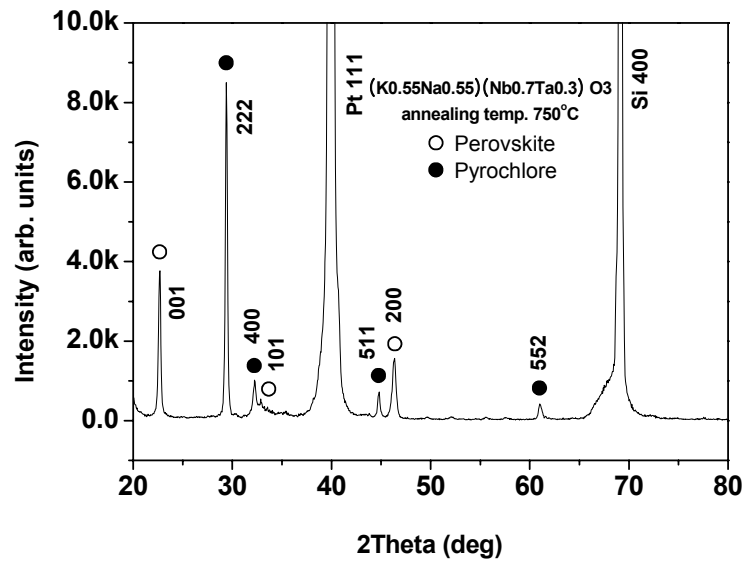
Figure 4.16 XRD patterns of KNNT thin films annealed at 750°C. The peak identities were excerpted by reference [73].

As might be expected, the pyrochlore phases cause severe leakage current at the P-E hysteresis loops as shown in Figure 4.17.
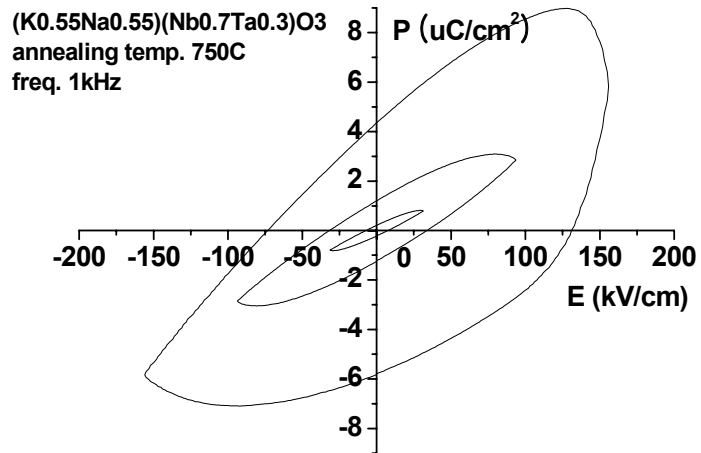
Figure 4.17 The P-E hysteresis loops of the 320nm thick KNN thin films annealed at 750°C with composition $(K_{0.55}Na_{0.55})(Nb_{0.7}Ta_{0.3})O_3$.

The second approach to reduce the leakage current was to improve homogeneity of KNN solution. There is a possible factor that the leakage current can stem from stains or defect on the surfaces of KNN thin films. When electric fields were applied to both electrodes of KNN capacitor structure, the carriers would migrate through such defects. The stains were observed in some KNN films as shown in Figure 4.18.
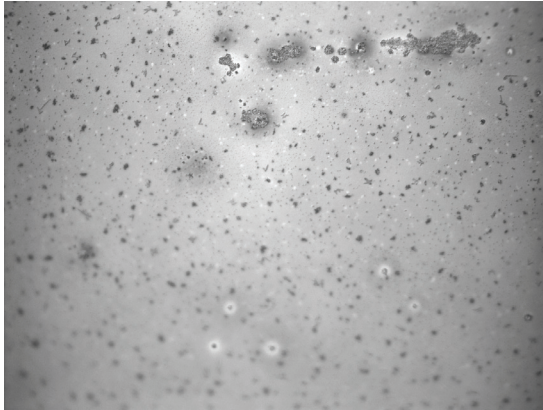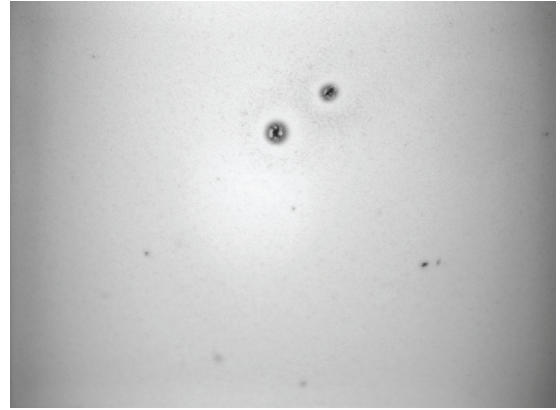
<center>(a)   (b)</center>

Figure 4.18 The optical micrographs of (a) KNN thin films with stains and (b) films without stains.

It was speculated that the solvent absolute ethanol would be better for the dissolution of sol-gel precursors in comparison with 2-MOE as discussed in the section 4.1. However, there was no discernible difference during solution preparation between the routes by 2-MOE and absolute ethanol. But P-E hysteresis loops seem to be worse as shown in Figure 4.19. The film does not withstand the field over 100 kV/cm, and the leakage current is not effectively reduced based on the unsaturated curve at the around maxium electric fields. Therefore, more careful solution process and detailed parametric studies should be performed in the future.
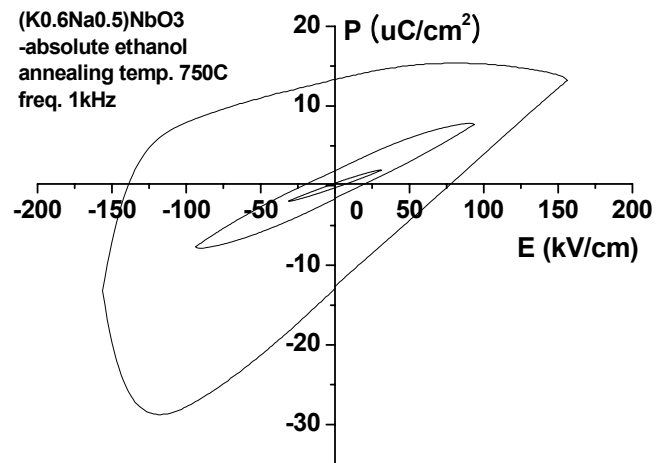
<center>74</center>

Figure 4.19 P-E hysteresis loops of KNN thin films fabricated by KNN solution dissolved

by absolute ethanol and AcAc.

CHAPTER V

SUMMARY AND CONCLUSIONS

A lead-free piezoelectric material $(K_{0.5}Na_{0.5})NbO_3$ (KNN) was fabricated by sol-gel processing. Crystalline KNN thin films were grown from temperatures as low as 550 ºC on Pt(111)/SiO$_2$/Si(100) and SiO$_2$/Si(100) substrates. The effects of substrate on the orientation of KNN films were not evident. However, the thickness of pyrolized film has a strong influence on the evolution of orientation and microstructure of these KNN films. The annealing of thinner pyrolized layers resulted in a textured orientation due to heterogeneous nucleation and growth from the interface between substrates and KNN, whereas for thicker layers, random orientation occurred by nucleation and growth from the inside of film bulk as depicted in the schematic diagram. For $(K_{0.5}Na_{0.5})NbO_3$ thin films, the proper P-E hysteresis loops could not be obtained due to volatilization of K and Na ions. To solve the problem, excessive Na and K ions were added to KNN solution, resulting in better saturation hysteresis, which may be due to reduction of defects that causes leaky behaviors of KNN thin films.

BIBLIOGRAPHY

1. Y. Saito, H. Takao, T. Tani, T. Nonoyama, K. Takatori, T. Homma, T. Nagaya, M. Nakamura, Nature 432 (2004) 84.

2. E. Cross, Nature 432 (2004) 24.

3. M.D. Maeder, D. Damjanovic, N. Setter, J. Electroceram. 13 (2004) 385.

4. T.R. Shrout, S.J. Zhang, J. Electroceram. 19 (2007) 111.

5. http://www.nlm.nih.gov/medlineplus/ency/article/002473.htm

6. K. Singh, V. Lingwal, S.C. Bhatt, N.S. Panwar, B.S. Semwal, Mater. Res. Bull. 36 (2001) 2365.

7. T. Saito, T. Wada, H. Adachi, I. Kanno, Jpn. J. Appl. Phys. 43 (2004) 6627.

8. C-R. Cho, A. Grishina, J. Appl. Phys. 87 (2000) 4439.

9. J. Ryu, J.J. Choi, B.D. Hahn, D.S. Park, W.H. Yoon, K.H. Kim, Appl. Phys. Lett. 90 (2007) 152901.

10. C-R. Cho, Mater. Lett. 57 (2002) 781.

11. X. Wang, S. Olafsson, L.D. Madsenc, S. Rudner, I.P. Ivanovd, A. Grishin, U. Helmersson, J. Mater. Res. 17 (2002) 1183.

12. S.I. Khartsev, M.A. Grishin, A.M. Grishin, Appl. Phys. Lett. 86 (2005) 062901.

13. M. Blomqvist, S. Khartsev, A. Grishin, Integr. Ferroelectr. 80 (2006) 97.

14. S.I. Khartsev, M.A. Grishin, A.M. Grishin, U.O. Karlsson, Integr. Ferroelectr. 80 (2006) 133.

15. V.M. Kuglera, F. Söderlind, D. Music, U. Helmersson, J. Andreasson, T. Lindbäck, J. Cryst. Growth. 262 (2004) 322.

16. H-J. Lee, C-W. Ahn, S-H. Kang, I-W. Kim, J-S. Lee, B-M. Jin, Ferroelectrics. 335 (2006) 227.

17. K. Tanaka, H. Hayashi, K. Kakimoto, H. Ohsato, T. Iijima, Jpn. J. Appl. Phys. 46 (2007) 6964.

18. K. Tanaka, K. Kakimoto, H. Ohsato, J. Cryst. Growth. 294 (2006) 209.

19. Y. Nakashima, W. Sakamoto, T. Shimura, T. Yogo, Jpn. J. Appl. Phys. 46 (2007) 6971.

20. Y. Nakashima, W. Sakamoto, H. Maiwa, T. Shimura, T. Yogo, Jpn. J. Appl. Phys. 46 (2007) L311.

21. Kwan Chi Kao, "Dielectric Phenomena in Solids", Elsevier 2004.

22. G. Haertling and C. Land, J. Am. Ceram. Soc., *54*, 1 (1971).

23. S. Liu, S. Pai, and J. Kyonka, Ferroelectrics, *22*, 689 (1978).

24. K. Okazaki, Ferroelectrics, *35*, 173 (1981).

25. M. Multani, S. Gokarn, R. Vijayaraghavan, and V. Polkar, Ferroelectrics, *37*, 652 (1981).

26. N. Murayama, T. Oikawa, T. Katto, and K. Nakamura, J. Polym. Sci. Polym. Phys. Ed. *13*, 1033 (1975).

27. N. Murayama and Hazhizume, J. Polym. Sci. Polym. Phys. Ed. *14*, 989 (1976).

28. T. Furukawa, K. Ishida, and E. Fukada, J. Appl. Phys. *50*, 4904 (1979).

29. K. Uchino, piezoelectric Actuators and Ultrasonic Motors, (Kluwer Academic, Boston, 1996).

30. K. Uchino, Ferroelectrics, 91, 281 (1989).

31. K Uchino, "Ceramic Actuators: Principles and Applications," (MRS Bulletin, April 1993), p. 42.

32. J.G. Smith and W.S. Choi, IEEE Trans. Ultrason., Ferroelect., Freq. Contr. 38, 256 (1991)

33. Q.M. Wang, X.H. Du, B.M. Xu, and L.E. Cross, IEEE Trans. Ultrason., Ferroelect., Freq. Contr. 46, 638 (1999)

34. R.E. Jaeger, and L. Egerton, J. Am. Ceram. Soc. **45**, 209–213 (1962)

35. G.H. Haertling, J. Am. Ceram. Soc. **50**, 329–330 (1967)

36. Thomas R. Shrout, and Shujun J. Zhang, J Electroceram DOI 10.1007/s10832-007-9047-0

37. J.F. Li, K. Wang, B.P. Zhang, and L.M. Zhang, J. Am. Ceram. Soc. **89**, 706–709, (2006)

38. B.P. Zhang, J.F. Li, K. Wang, and H. Zhang, J. Am. Ceram. Soc. **89**, 1605–1609 (2006)

39. G. Arlt, D. Hennings, and G. de With, J. Appl. Phys. **58**, 1619–1625, (1985)

40. Y. Saito, H. Takao, T. Tani, T. Nonoyama, K. Takatori, T. Homma, T. Nagaya, M. Nakamura, Nature **432**, 84–87 (2004)

41. E. Hollenstein, M. Davis, D. Damjanovic, N. Setter, Appl. Phys. Lett. **87**, 182905 (2005)

42. Y. Saito, H. Takao, Ferroelectrics **338**, 17–32 (2006)

43. R. Wang, R. Xie, K. Hanada, K. Matsusaki, H. Bando, M. Itoh, Phys. Status Solidi, A Appl. Res. **202**, R57–R59 (2005)

44. R. Wang, R.J. Xie, K. Hanada, K. Matsusaki, H. Bando, T. Sekiya, M. Itoh, Ferroelectrics **336**, 39–46 (2006)

45. Y. Guo, K. Kakimoto, H. Ohsato, Mater. Lett. **59**, 241–245 (2005)

46. Y. Guo, K. Kakimoto, H. Ohsato, Appl. Phys. Lett. **85**, 4121–4123 (2004)

47. B. Jaffe, W. Cook, H. Jaffe, *Piezoelectric Ceramics* (Academic, NY, 1971), p. 92

48. S.J. Zhang, R. Xia, T.R. Shrout, *J. Electroceramics*. (in press)

49. R. Wang, R. Xie, K. Hanada, K. Matsusaki, H. Bando, M. Itoh, Phys. Status Solidi, A Appl. Res. 202, R57–R59 (2005)

50. R. Wang, R.J. Xie, K. Hanada, K. Matsusaki, H. Bando, T. Sekiya, M. Itoh, Ferroelectrics 336, 39–46 (2006)

51. Y. Guo, K. Kakimoto, H. Ohsato, Mater. Lett. 59, 241–245 (2005)

52. Y. Guo, K. Kakimoto, H. Ohsato, Appl. Phys. Lett. 85, 4121–4123 (2004)

53. S.J. Zhang, R. Xia, T.R. Shrout, G.Z. Zang, J.F. Wang, J. Appl. Phys. 100, 104108 (2006)

54. MS Bhuiyan, M Paranthaman and K Salama, "Solution-derived textured oxide thin films—a review", Supercond. Sci. Technol. **19** (2006) R1–R21

55. Fukushima J, Kodaira K and Matsushita T 1984 *J. Mater. Sci.* **19** 595

56. Budd K D, Dey S K and Payne D A 1985 *Brit. Ceram. Soc. Proc.* **36** 107

57. Dey S K, Budd K D and Payne D A 1988 *IEEE Trans. UFFC* **35** 80

58. Otsuki T and Arita K 1997 *Integr. Ferroelectr.* **17** 31

59. Yi G and Sayer M 1991 *Ceram. Bull.* **70** 1173

60. Takehisa Saito, Takahiro Wada, Hideaki Adachi and Isaku Kanno, Jpn. J. Appl. Phys. 43 (2004) 6627–6631.

61. Takehisa Saito, Harumi Adachi, Takahiro Wada and Hideaki Adachi, Jpn. J. Appl. Phys. 44 (2005) 6969–6972

62. Xin Wang, Sveinn Olafsson, and Lynnette D. Madsen, J. Mater. Res., Vol. 17, No. 5, May 2002.

63. Veronika M. Kugler, Fredrik Söderlind, Denis Music, Ulf Helmersson, Johanna Andreasson, Ture Lindbäck, Journal of Crystal Growth 262 (2004) 322 – 326.

64. Isaku Kanno, Takuya Mino, Shuichiro Kuwajima, Takaaki Suzuki, Hidetoshi Kotera, and Kiyotaka Wasa, IEEE transactions on ultrasonics, ferroelectrics, and frequency control, Vol. 54, No. 12, December 2007.

65. A. Fredrik Söderlind, Per-Olov Käll, Ulf Helmersson, Journal of Crystal Growth 281 (2005) 468–474

66. Ken-ichi Kakimoto, Koichiro Akao, Yiping Guo and Hitoshi Ohsato, "Raman Scattering Study of Piezoelectric $(Na_{0.5}K_{0.5})NbO_3$-$LiNbO_3$ Ceramics", Jpn. J. Appl. Phys. Vol. 44, No. 9B, 2005, pp. 7064–7067

67. X.J. Meng, J.G. Cheng, J.L. Sun, J. Tan, H.J. Ye, J.H. Chu, Thin Solid Films. 368 (2000) 22.

68. F. Lai, J-F. Li, J. Sol-Gel. Sci. Techn. 42 (2007) 287.

69. Title : Refractory for Black Liquor Gasifiers / Type of Report: Quarterly Report / Reporting Period Start Date: October 1, 2002 / Reporting Period End Date: June 30, 2003 / Principal Authors: William L. Headrick Jr. and Alireza Rezaie / Date Report Issued : August 2003 / DOE Award Number : DE-FC26-02NT41491.

70. American Chemical Society & American Institute of Physics & National Institute of Standards and Technology. NIST-JANAF Thermochemical Tables, 4th Edition, New York, 1998.

71. Yoichi Kizaki, Yuji Noguchi, and Masaru Miyayama, "Defect control for low leakage current in $K_{0.5}Na_{0.5}NbO_3$ single crystals", Appl. Phys. Lett. **89**, 142910 (2006).

72. Masato Matsubara, Toshiaki Yamaguchi, Koichi Kikuta and Shin-ichi Hirano, "Synthesis and Characterization of $(K_{0.5}Na_{0.5})(Nb_{0.7}Ta_{0.3})O_3$ Piezoelectric Ceramics Sintered with Sintering Aid $K_{5.4}Cu_{1.3}Ta_{10}O_{29}$", Japanese Journal of Applied Physics Vol. 44, No. 9A, 2005, pp. 6618–6623.

73. C. J. Lu, A. X. Kuang, "Preparation of potassium tantalate niobate through sol–gel processing", Journal of Materials Science 32 (1997) pp. 4421 - 4427.